POGGIO LAB

Nanomagnetic Imaging using Scanning Probe Microscopy Techniques

PhD Course:

"Advanced microscopy techniques for characterizing magnetic properties of materials"

17.11.2022

Prof. Martino Poggio

Based on *Nat. Rev. Phys.* **4**, 49 (2022).

Faraday's iron filings

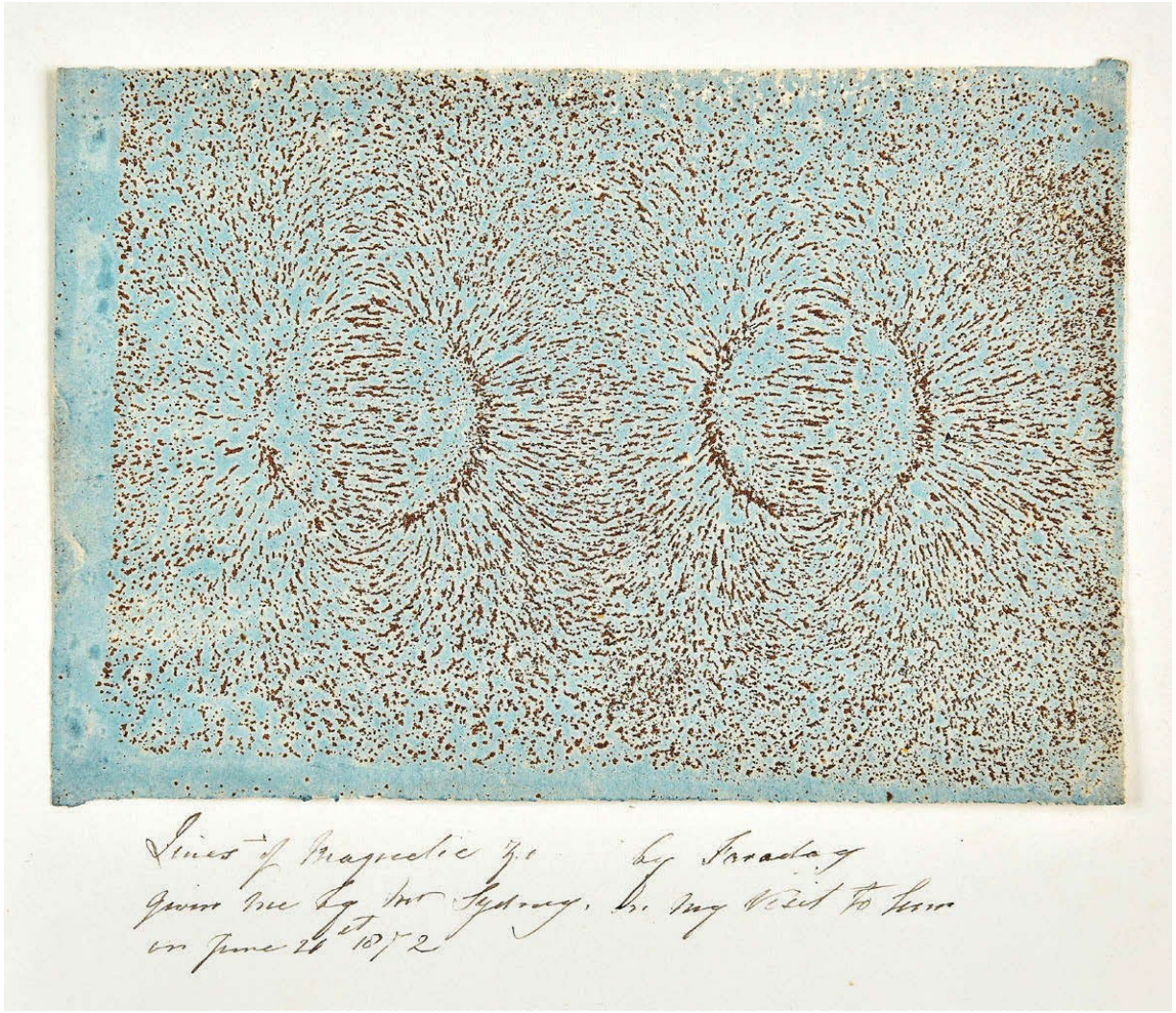

M. Faraday, ca. 1830s

Scanning tunnelling spectroscopy on atomic-scale

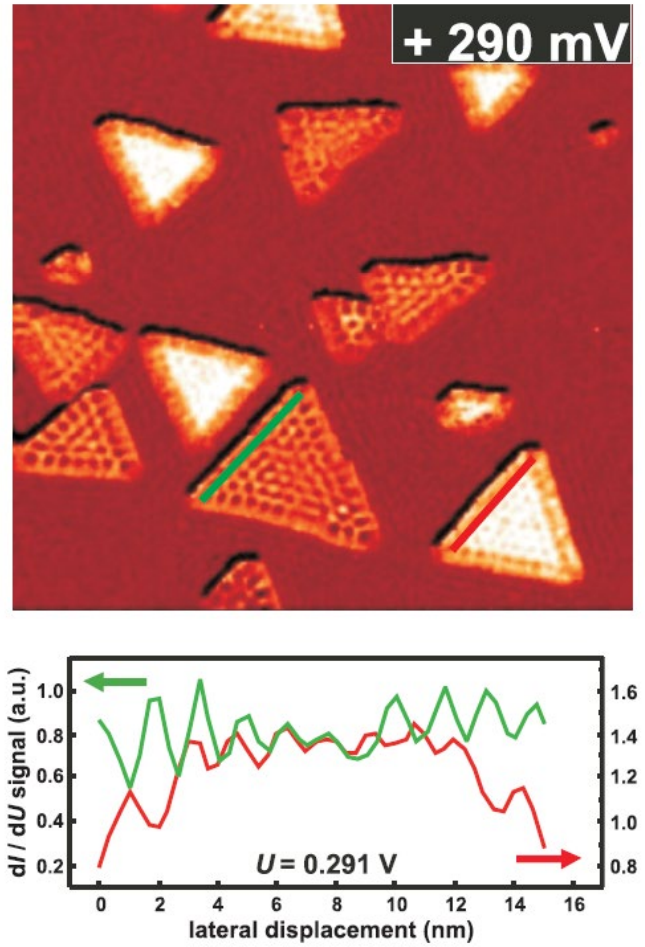

FIG. 44. (Color) SP-STS data (60×60 nm^2) revealing the spin dependence of the 2D electronic confinement states in nano-scale Co islands which manifests itself by a spin-dependent oscillation amplitude of the confinement states for differently magnetized Co nanoislands. From Pietzsch *et al.*, 2006.

Magneto-optical imaging of local spin-polarization

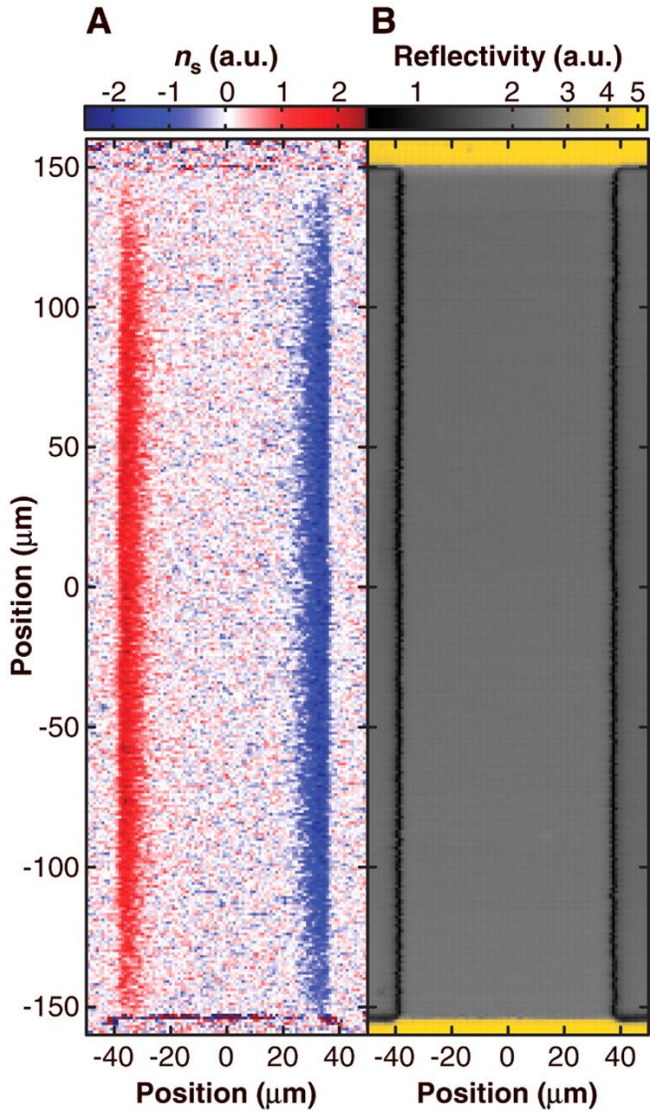

Kato et al., *Science* **306**, 5703 (2004).

Lorentz microscopy of skyrmion crystals

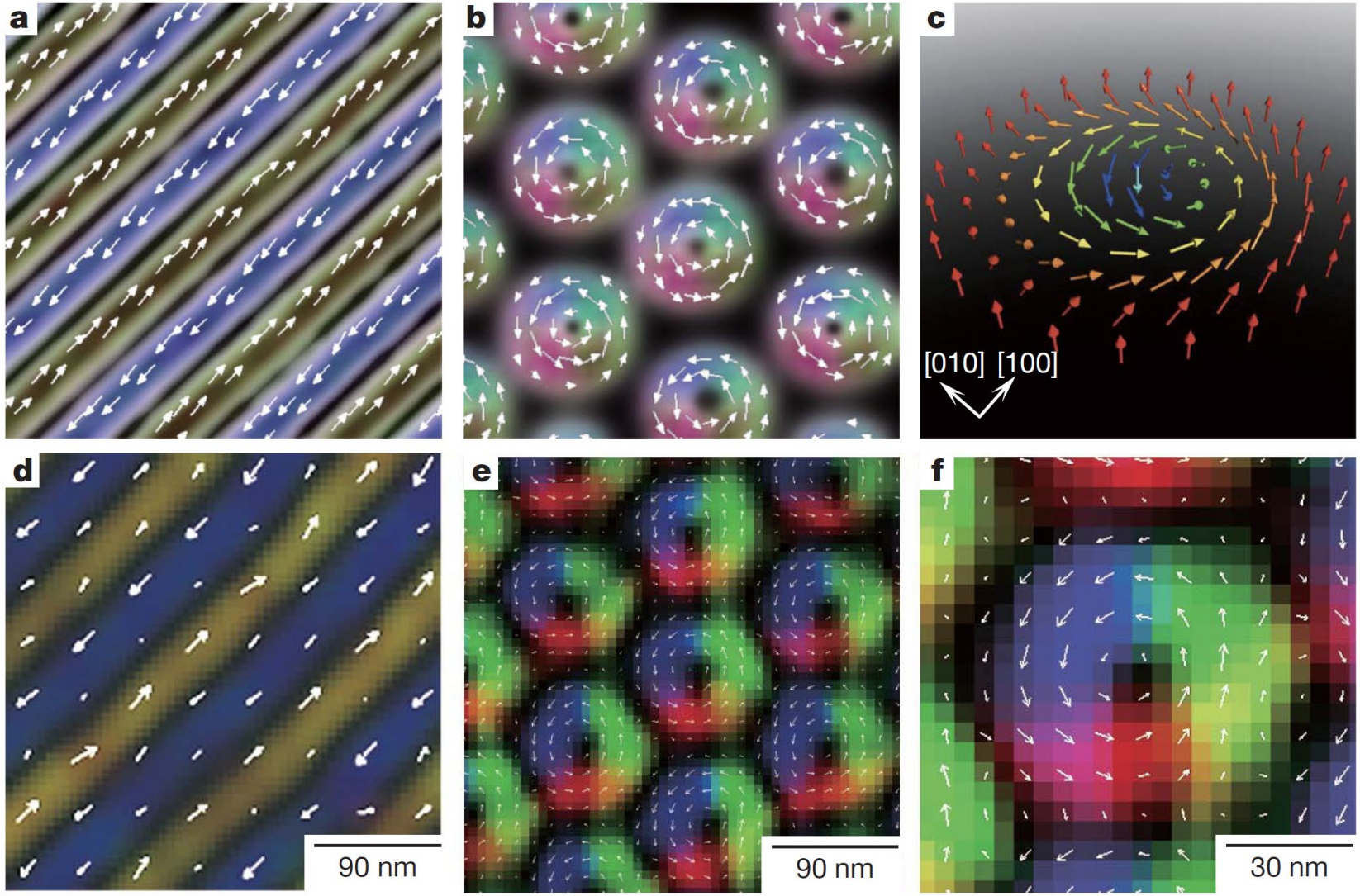

Yu et al., *Nature* **465**, 901 (2010).

SQUID microscopy of edge currents

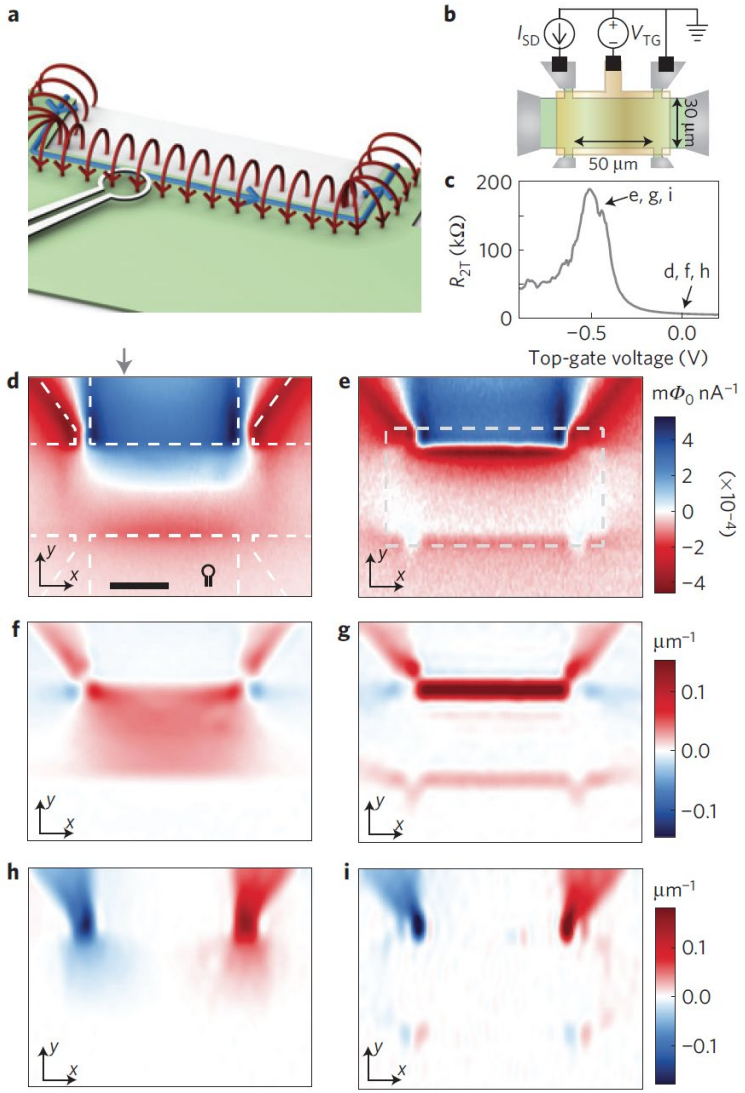

Nowack et al., *Nat. Phys.* **12**, 787 (2013).

Energence of 2D materials and vdW heterostructures

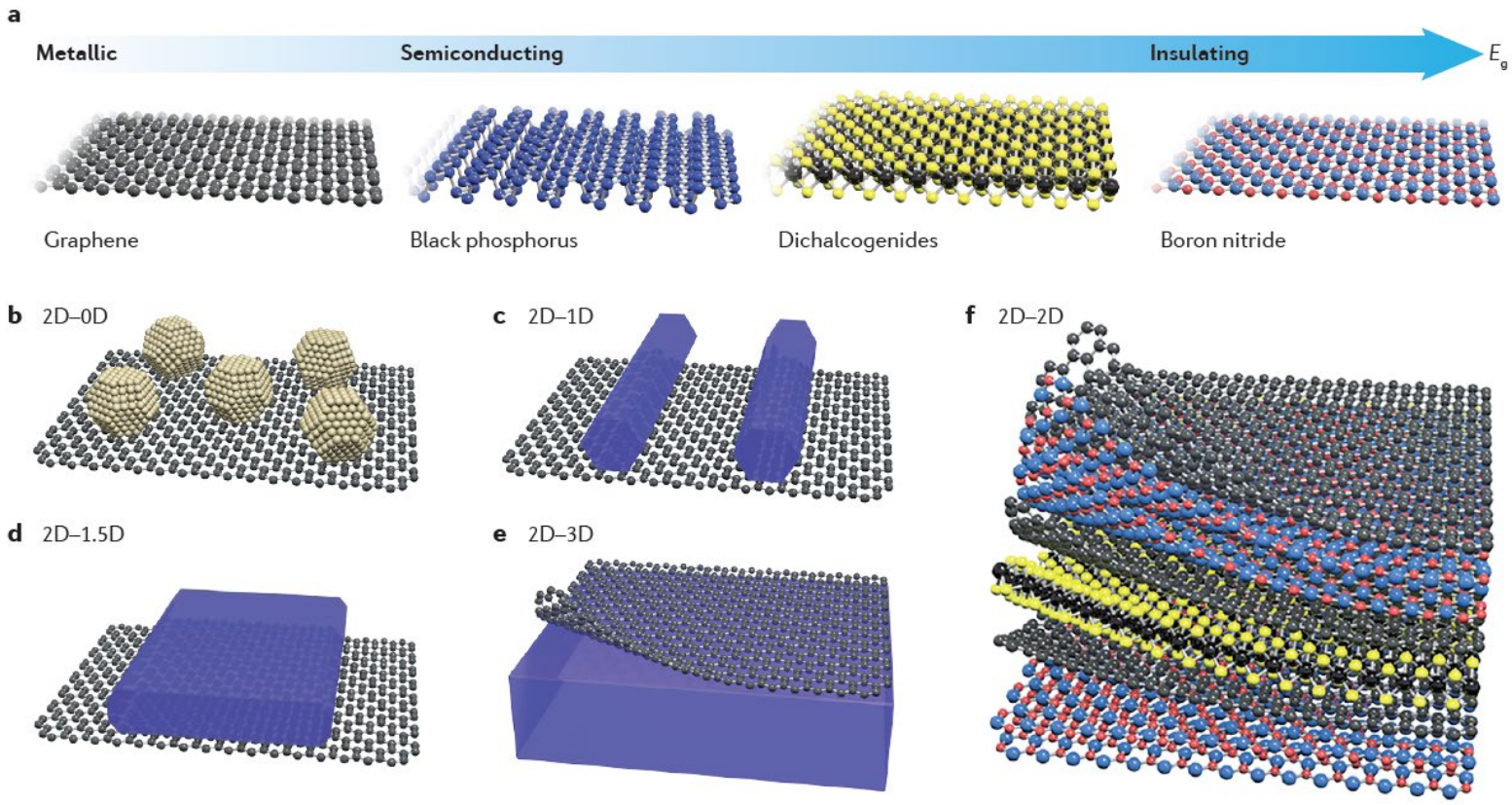

Figure 1 | **Two-dimensional layered materials and van der Waals heterostructures. a** | A broad library of two-dimensional layered materials (2DLMs) with varying chemical composition, atomic structures and electronic properties, with an increasing bandgap from left to right. **b**–**f** | Van der Waals heterostructures formed by integrating the dangling-bond-free 2DLMs with 0D nanoparticles or quantum dots (panel **b**), 1D nanowires (panel **c**), 1.5D nanoribbons (panel **d**), 3D bulk materials (panel **e**) and 2D nanosheets (panel **f**).

Liu et al., *Nat. Rev. Mater.* **1**, 1 (2016)

Energence of 2D materials and vdW heterostructures

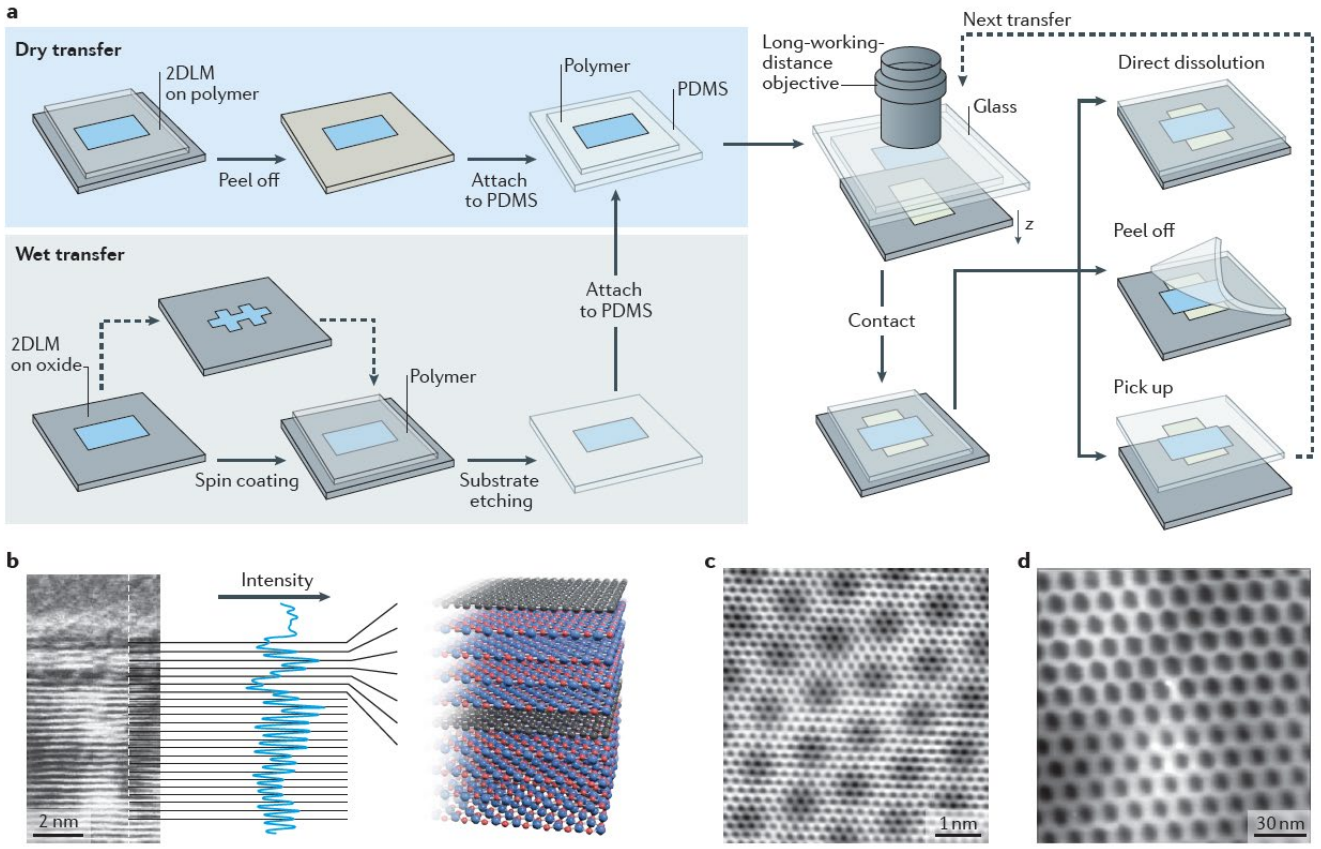

Figure 2 | **Assembly and characterization of 2D–2D vdWHs. a** | Schematic illustration of state-of-the-art alignment transfer processes for van der Waals heterostructure (vdWH) integration. Wet and dry transfer techniques are used to attach the target sheet to the stamp material. The stamp is then attached to a glass slide and placed in a transfer microscope. Micromanipulators allow for the precise alignment of sheets using a long-working-distance objective lens. The polymer transfer stamp can either be chemically dissolved away, mechanically peeled off or used to pick up the entire stack for further transfer steps. **b** | False-coloured high-resolution cross-sectional scanning tunnelling electron microscopy image of the BN–graphene–BN–graphene stack (left) and a corresponding schematic representation (right). **c**,**d** | Moiré pattern of graphene on BN (panel **c**) and a much larger moiré pattern of the commensurate–incommensurate transition of graphene on BN (panel **d**). 2DLM, two-dimensional layered material; BN, boron nitride; PDMS, poly(dimethyl siloxane). Panel **b** is from REF. 71, Nature Publishing Group. Panel **c** is courtesy of Brian LeRoy, University of Arizona, USA. Panel **d** is from REF. 73, Nature Publishing Group.

Liu et al., *Nat. Rev. Mater.* **1**, 1 (2016)

Correlated states in atomically layered materials

ARTICLE

doi:10.1038/nature26160

Unconventional superconductivity in magic-angle graphene superlattices

Yuan Cao[1], Valla Fatemi[1], Shiang Fang[2], Kenji Watanabe[3], Takashi Taniguchi[3], Efthimios Kaxiras[2,4] & Pablo Jarillo-Herrero[1]

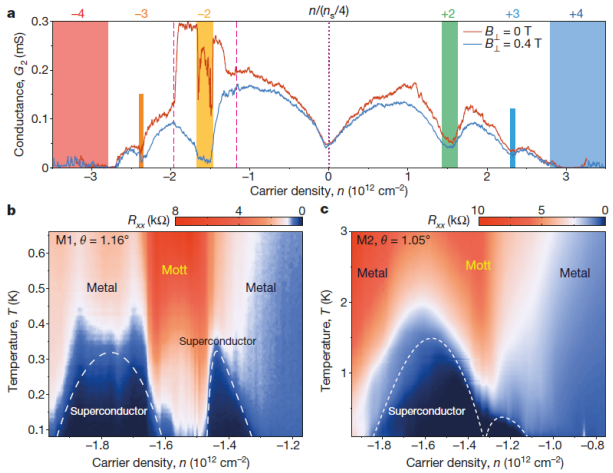

Figure 2 | Gate-tunable superconductivity in magic-angle TBG. **a**, Two-probe conductance $G_2 = I/V_{bias}$ of device M1 ($\theta = 1.16°$) measured in zero magnetic field (red) and at a perpendicular field of $B_\perp = 0.4$ T (blue). The curves exhibit the typical V-shaped conductance near charge neutrality ($n = 0$, vertical purple dotted line) and insulating states at the superlattice bandgaps $n = \pm n_s$, which correspond to filling ± 4 electrons in each moiré unit cell (blue and red bars). They also exhibit reduced conductance at intermediate integer fillings of the superlattice owing to Coulomb interactions (other coloured bars). Near a filling of -2 electrons per unit cell, there is considerable conductance enhancement at zero field that is suppressed in $B_\perp = 0.4$ T. This enhancement signals the onset of superconductivity. Measurements were conducted at 70 mK; $V_{bias} = 10\,\mu$V. **b**, Four-probe resistance R_{xx}, measured at densities corresponding to the region bounded by pink dashed lines in **a**, versus temperature. Two superconducting domes are observed next to the half-filling state, which is labelled 'Mott' and centred around $-n_s/2 = -1.58 \times 10^{12}$ cm^{-2}. The remaining regions in the diagram are labelled as 'metal' owing to the metallic temperature dependence. The highest critical temperature observed in device M1 is $T_c = 0.5$ K (at 50% of the normal-state resistance). **c**, As in **b**, but for device M2, showing two asymmetric and overlapping domes. The highest critical temperature in this device is $T_c = 1.7$ K.

LETTER

doi:10.1038/nature22391

Layer-dependent ferromagnetism in a van der Waals crystal down to the monolayer limit

Bevin Huang[1]*, Genevieve Clark[2]*, Efrén Navarro-Moratalla[3]*, Dahlia R. Klein[3], Ran Cheng[4], Kyle L. Seyler[1], Ding Zhong[1], Emma Schmidgall[1], Michael A. McGuire[5], David H. Cobden[1], Wang Yao[6], Di Xiao[4], Pablo Jarillo-Herrero[3] & Xiaodong Xu[1,2]

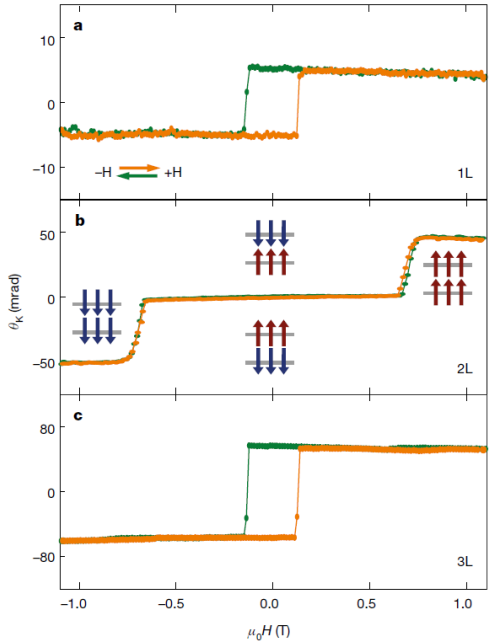

Figure 3 | Layer-dependent magnetic ordering in atomically-thin CrI_3. **a**, MOKE signal on a monolayer (1L) CrI_3 flake, showing hysteresis in the Kerr rotation as a function of applied magnetic field, indicative of ferromagnetic behaviour. **b**, MOKE signal from a bilayer CrI_3 showing vanishing Kerr rotation for applied fields ± 0.65 T, suggesting antiferromagnetic behaviour. Insets depict bilayer (2L) magnetic ground states for different applied fields. **c**, MOKE signal on a trilayer (3L) flake, showing a return to ferromagnetic behaviour.

How to decipher the mechanism behind these phenomena?

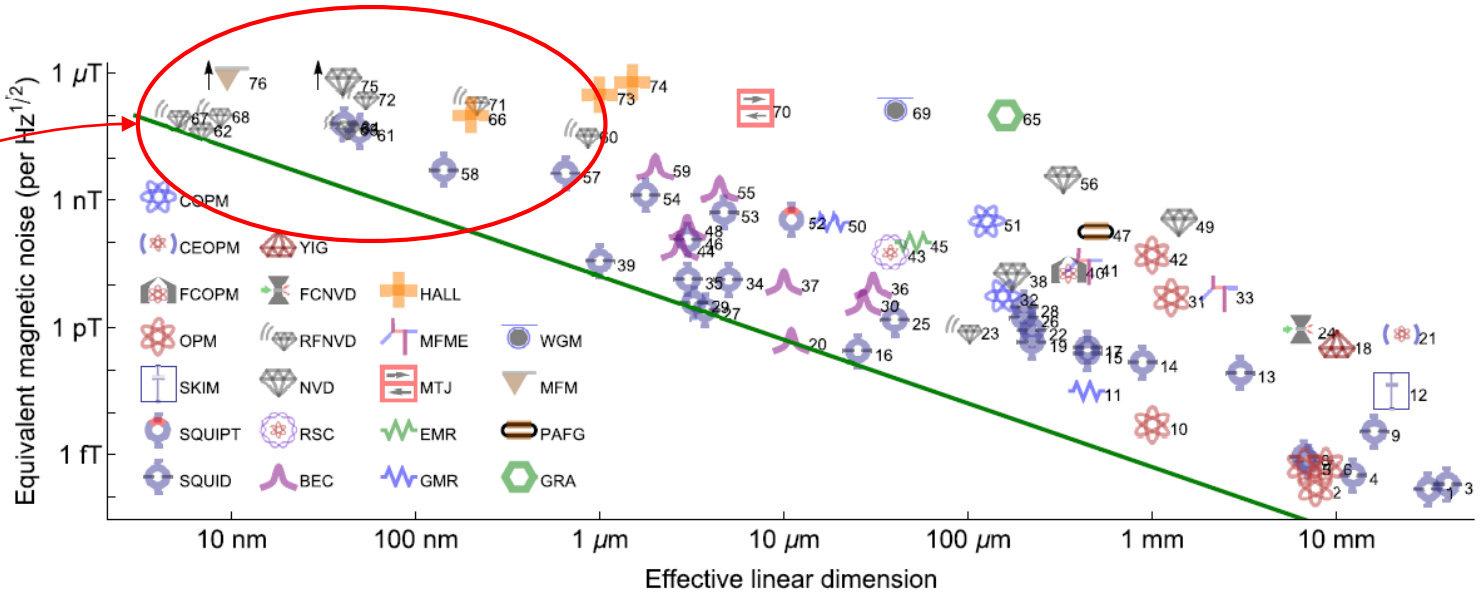

FIG. 2. Reported magnetic sensitivity $\delta B\sqrt{T}$ for different sensor technologies versus size of the sensitive region. Effective linear dimension l_{eff} indicates $\sqrt{\text{area}}$ for planar sensors and $\sqrt[3]{\text{volume}}$ for volumetric ones. For pointlike systems such as single spins, l_{eff} indicates $\sqrt[3]{\text{volume}}$ for a sphere with radius equal to the minimum source-detector distance. For work reporting sensitivity in units of magnetic dipole moment, we convert to field units using the reported sample distance. Excepting RFNVD, noise levels are the lowest reported value at frequency ≤ 1 kHz. An arrow indicates that the value is off the scale. SQUID, superconducting quantum interference device; SQUIPT, superconducting quantum interference proximity transistor; SKIM, superconducting kinetic impedance magnetometer; OPM, optically pumped magnetometer; FCOPM, OPM with flux concentrators; CEOPM, cavity-enhanced OPM; COPM, OPM with cold thermal atoms; BEC, Bose-Einstein condensate; RSC, Rydberg Schrödinger cat; NVD, nitrogen-vacancy center in diamond; RFNVD, radio-frequency NVD; FCNVD, NVD with flux concentrators; YIG, yttrium-aluminum-garnet; GMR, giant magnetoresistance; EMR, extraordinary magnetoresistance; MTJ, magnetic tunnel junction; MEMF, magnetoelectric multiferroic; HALL, Hall-effect sensor; GRA, graphene; PAFG, parallel gating fluxgate; MFM, magnetic force microscope, WGM, whispering-gallery mode magnetostrictive. Line shows $E_R \equiv \langle \delta B^2 \rangle T l_{\text{eff}}^3/(2\mu_0) = \hbar$. Numeric labels refer to Table I.

Map weak magnetic field patterns with high spatial resolution

Mitchell & Palacios Alvarez, *Rev. Mod. Phys.* **92**, 021001 (2020)

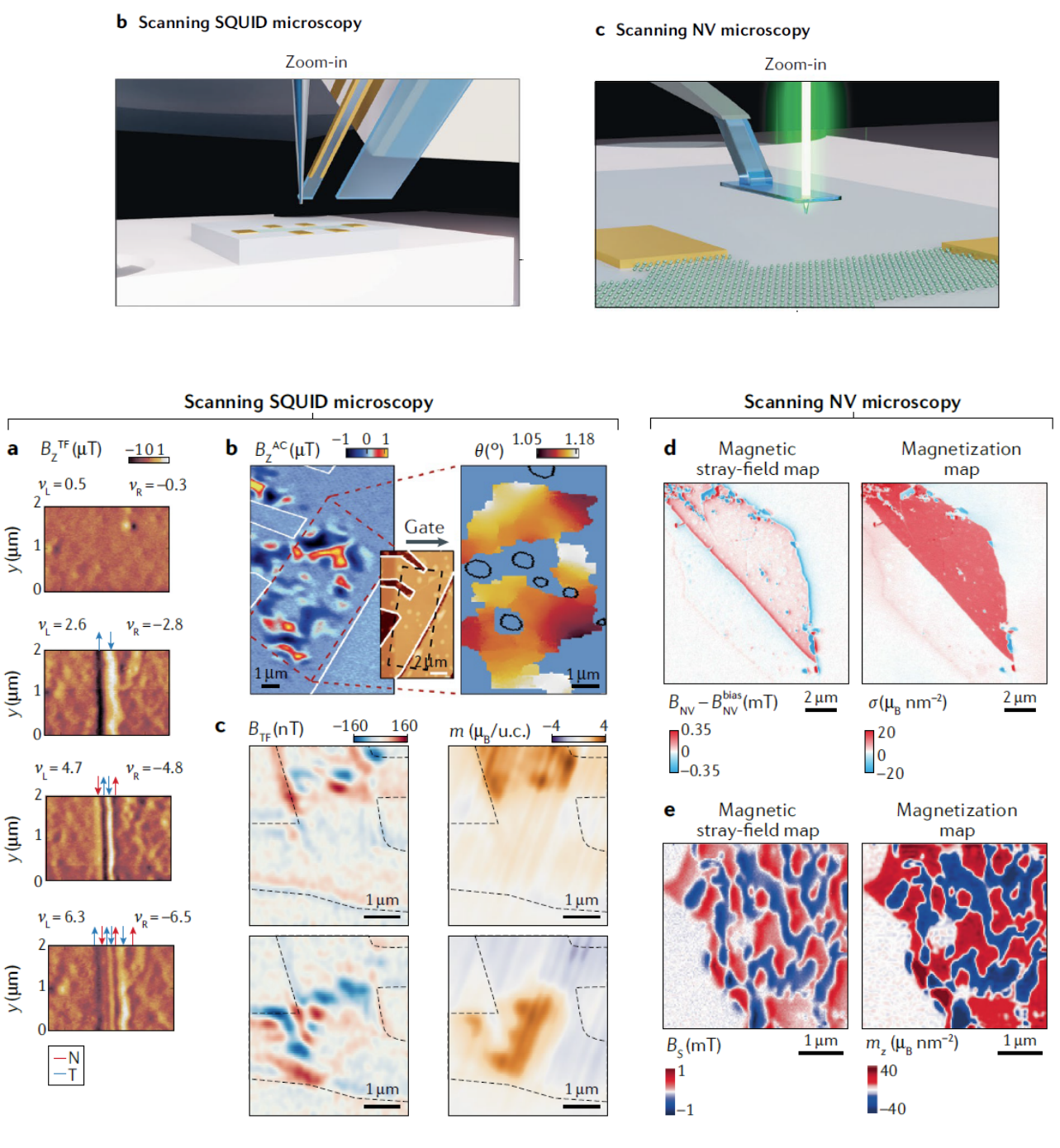
b Scanning SQUID microscopy
Zoom-in
c Scanning NV microscopy
Zoom-in
Scanning SQUID microscopy
Scanning NV microscopy
a
B_Z^{TF} (μT)
−1 0 1
$\nu_L = 0.5$
$\nu_R = -0.3$
$\nu_L = 2.6$
$\nu_R = -2.8$
$\nu_L = 4.7$
$\nu_R = -4.8$
$\nu_L = 6.3$
$\nu_R = -6.5$
y (μm)
N
T
b
B_Z^{AC} (μT)
−1 0 1
θ(°)
1.05 1.18
Gate
1 μm
2 μm
c
B_{TF} (nT)
−160 160
m (μ_B/u.c.)
−4 4
d
Magnetic stray-field map
Magnetization map
$B_{NV} - B_{NV}^{bias}$ (mT)
0.35
0
−0.35
σ(μ_B nm^{-2})
20
0
−20
e
Magnetic stray-field map
Magnetization map
B_S (mT)
1
−1
m_z (μ_B nm^{-2})
40
−40

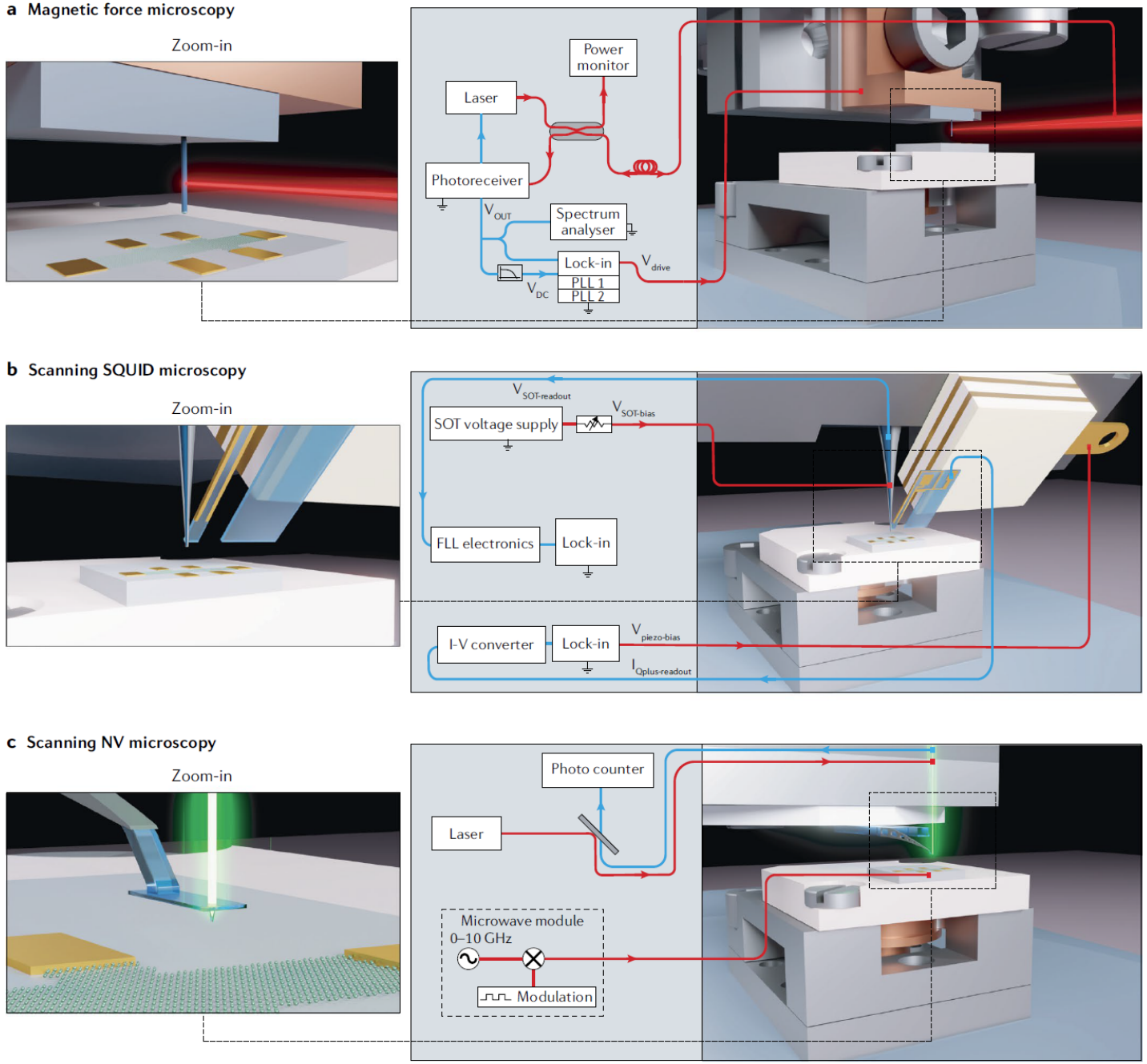
a Magnetic force microscopy
Zoom-in
Power monitor
Laser
Photoreceiver
V_{OUT}
Spectrum analyser
Lock-in
PLL 1
PLL 2
V_{drive}
V_{DC}
b Scanning SQUID microscopy
Zoom-in
$V_{SOT\text{-}readout}$
SOT voltage supply
$V_{SOT\text{-}bias}$
FLL electronics
Lock-in
I-V converter
Lock-in
$V_{piezo\text{-}bias}$
$I_{Qplus\text{-}readout}$
c Scanning NV microscopy
Zoom-in
Photo counter
Laser
Microwave module
0–10 GHz
Modulation

Idealized signal sources

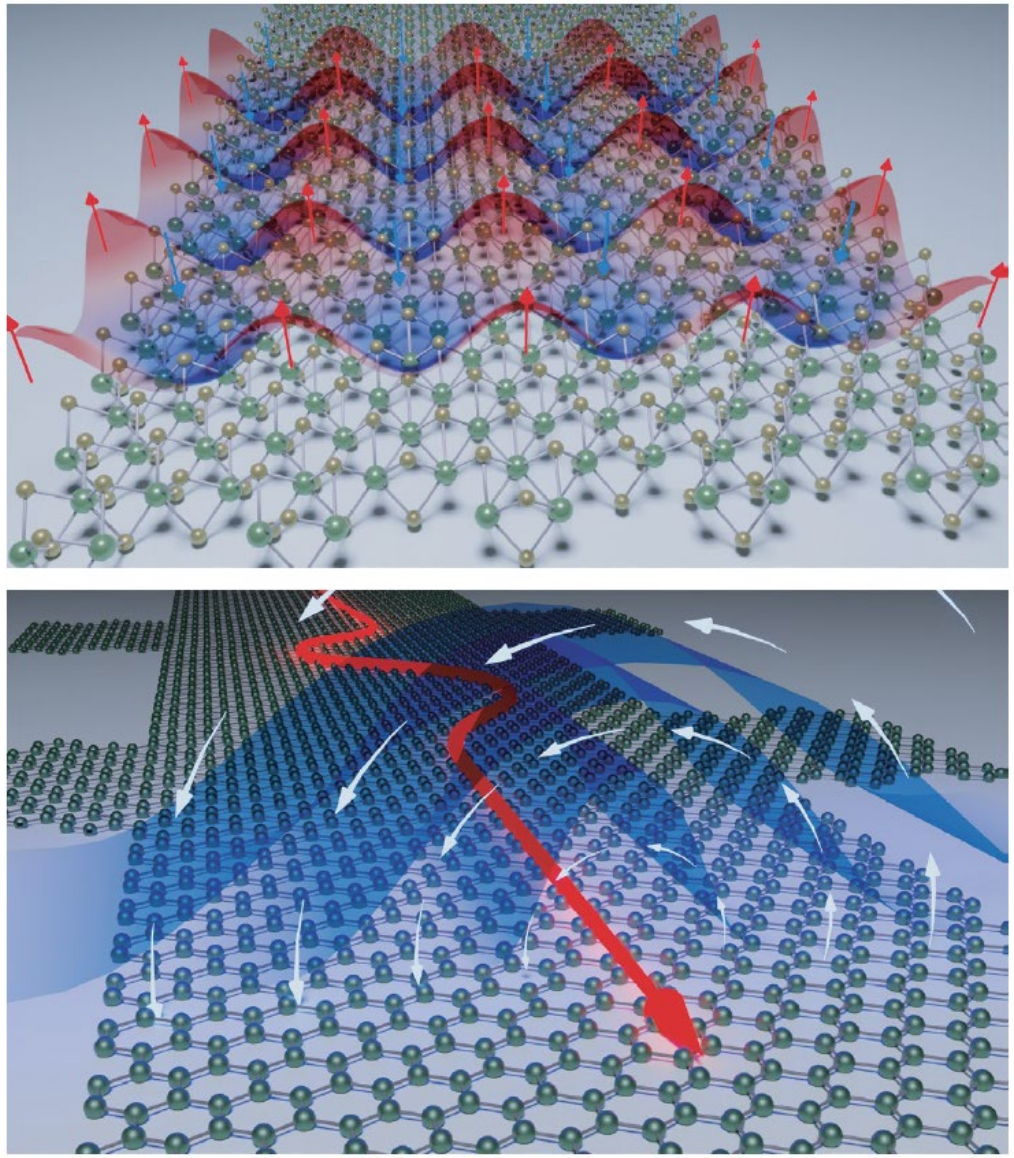

Magnetic imaging by "force microscopy" with 1000 Å resolution

Y. Martin and H. K. Wickramasinghe
IBM T. J. Watson Research Center, P. O. Box 218, Yorktown Heights, New York 10598

(Received 19 December 1986; accepted for publication 19 March 1987)

We describe a new method for imaging magnetic fields with 1000 Å resolution. The technique is based on using a force microscope to measure the magnetic force between a magnetized tip and the scanned surface. The method shows promise for the high-resolution mapping of both static and dynamic magnetic fields.

Appl. Phys. Lett. 50 (20), 18 May 1987

Magnetic force microscopy: General principles and application to longitudinal recording media

D. Rugar, H. J. Mamin, P. Guethner,[a] S. E. Lambert,[b] J. E. Stern,[c] I. McFadyen,[b] and T. Yogi[b]
IBM Research Division, Almaden Research Center, 650 Harry Road, San Jose, California 95120-6099

(Received 15 January 1990; accepted for publication 13 April 1990)

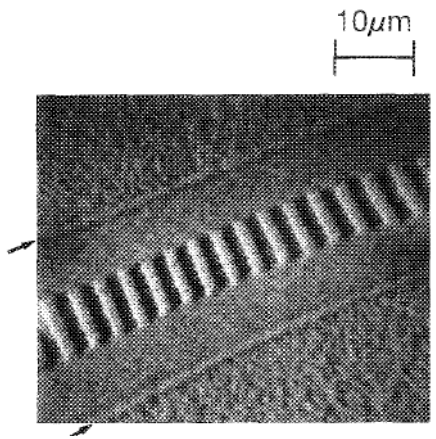

J. Appl. Phys. 68 (3), 1 August 1990

MFM achieves down to 10 nm resolution

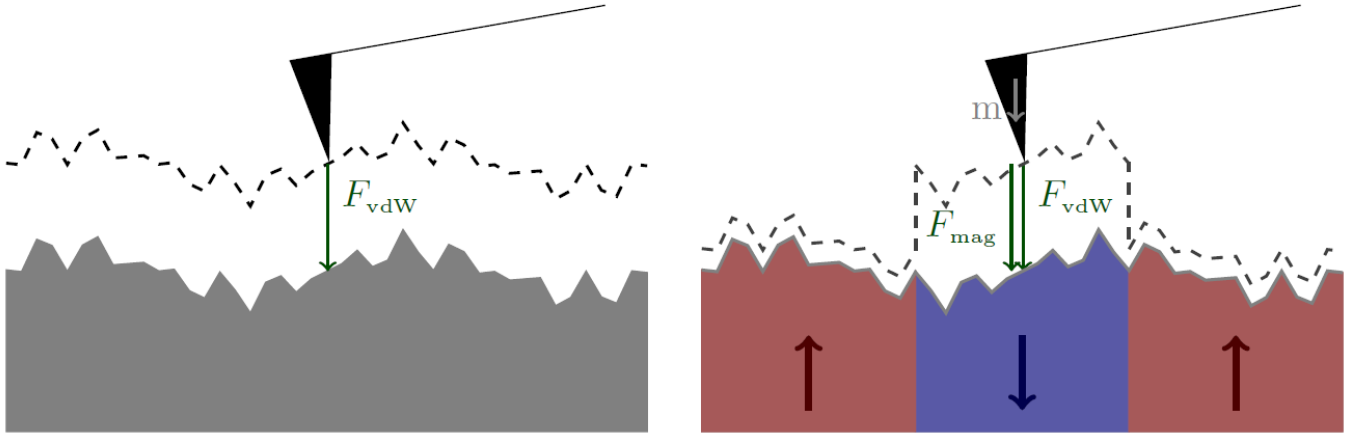

Schwenk, *Ph.D. Thesis in Physics,* University of Basel (2016).

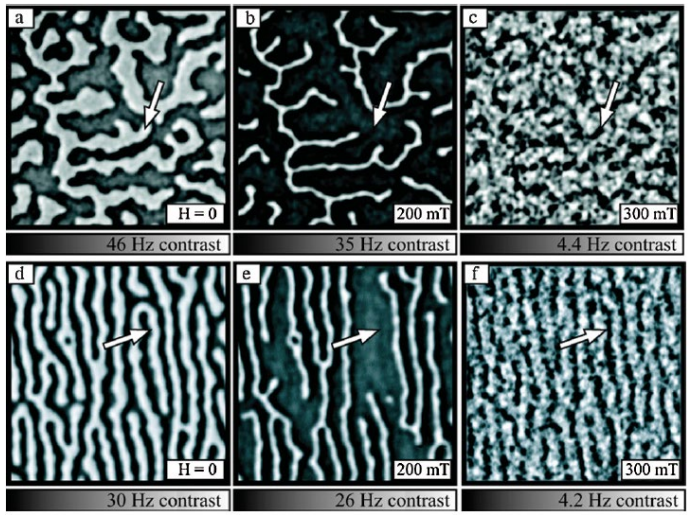

Schmid et al., *Phys. Rev. Lett.* **105**, 197201 (2010).

NWs with magnetic tips

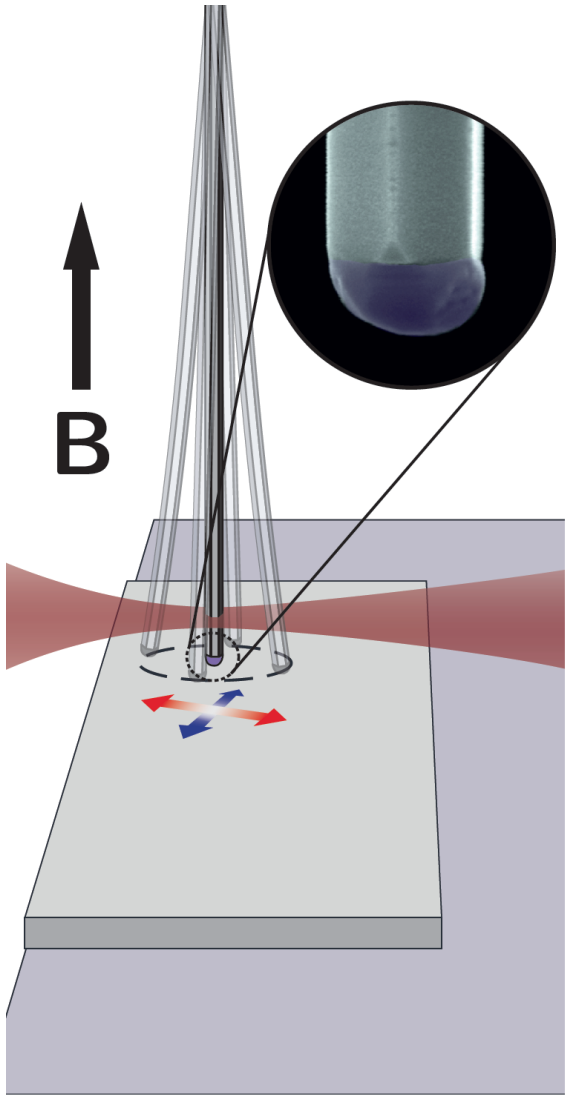

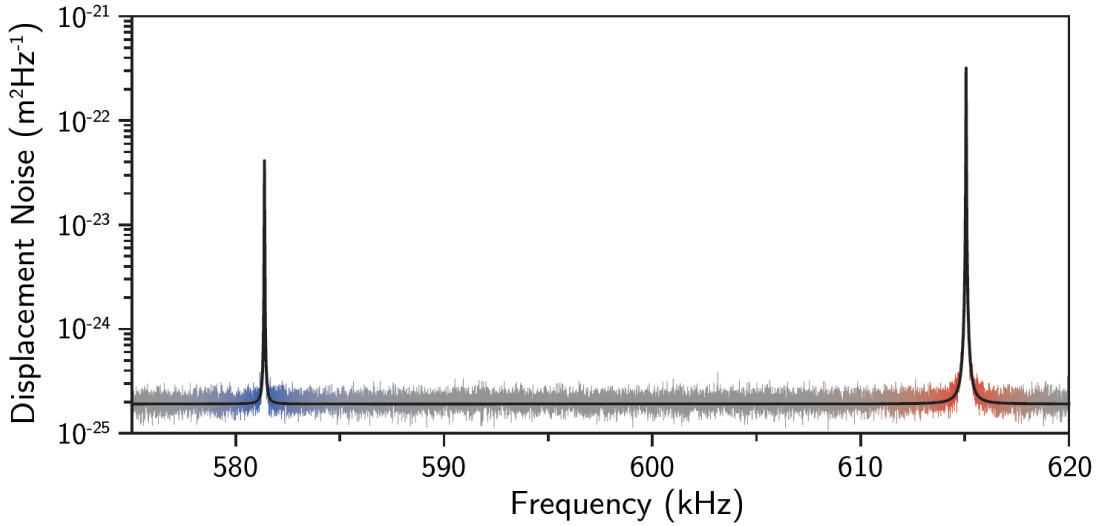

Length $\sim 17 \pm 1\,\mu$m with diameter $\sim 225 \pm 15$ nm

- $f \sim [500 - 700]$ kHz
- $Q \sim [30 - 50] \times 10^3$
- $k \sim [1 - 10]$ mN/m
- $M \sim 700$ fg
- $\Gamma \sim 50 \times 10^{-15}$ kg/s
- $F_{min} \sim 4$ aN/$\sqrt{\text{Hz}}$

Rossi et al., *Nano Lett.* **19**, 930 (2019).

MFM

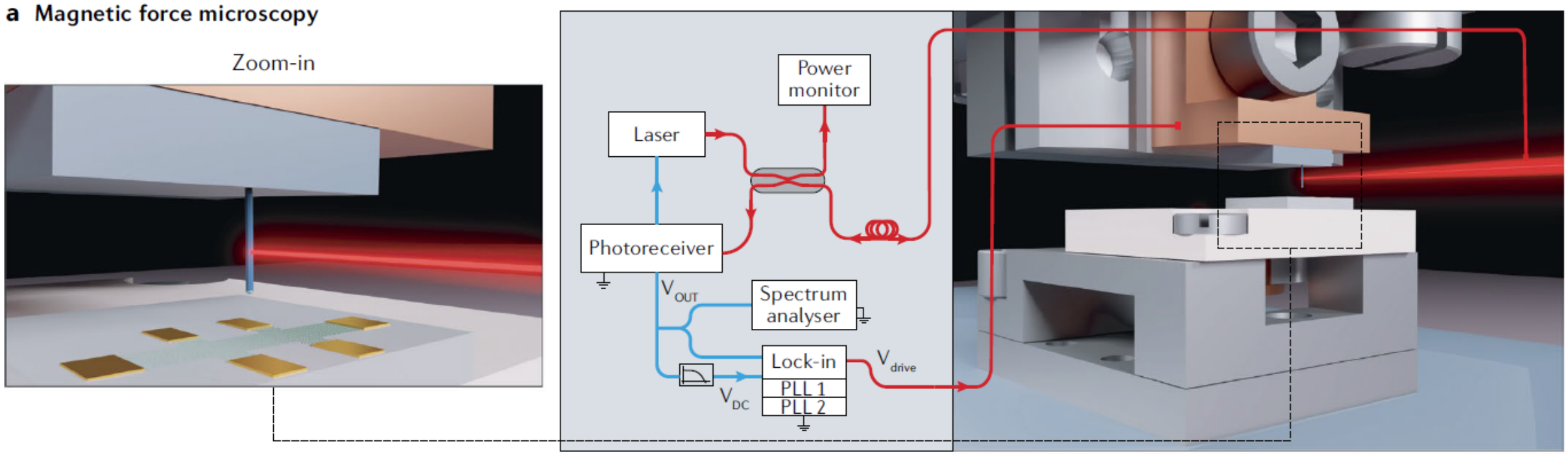
a Magnetic force microscopy
Zoom-in
Power monitor
Laser
Photoreceiver
V_{OUT}
Spectrum analyser
Lock-in
PLL 1
PLL 2
V_{drive}
V_{DC}

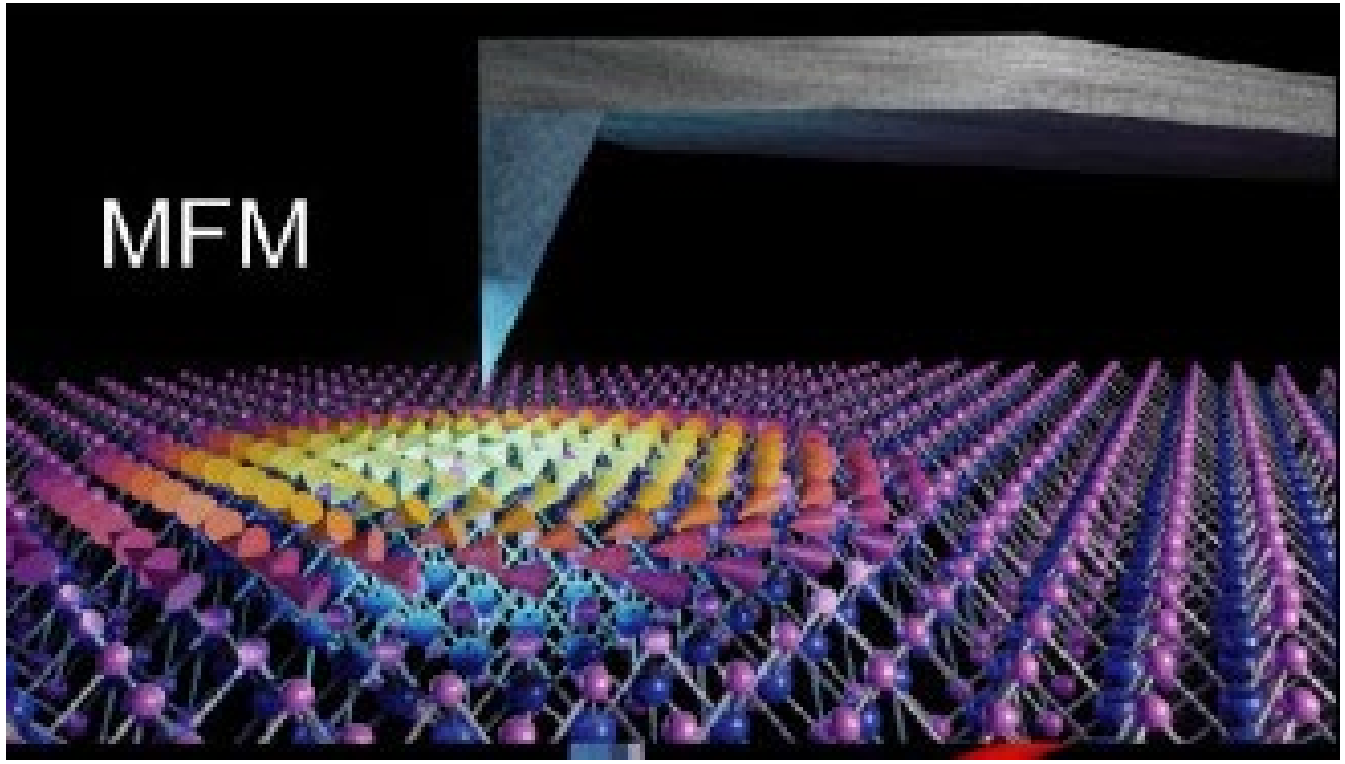
MFM

SCANNING SQUID MICROSCOPY

John R. Kirtley
IBM T. J. Watson Research Center, Yorktown Heights, New York 10598;
e-mail: kirtley@watson.ibm.com

John P. Wikswo, Jr.
Department of Physics and Astronomy, Vanderbilt University, Nashville,
Tennessee 37235; e-mail: wikswojp@ctrvax.vanderbilt.edu

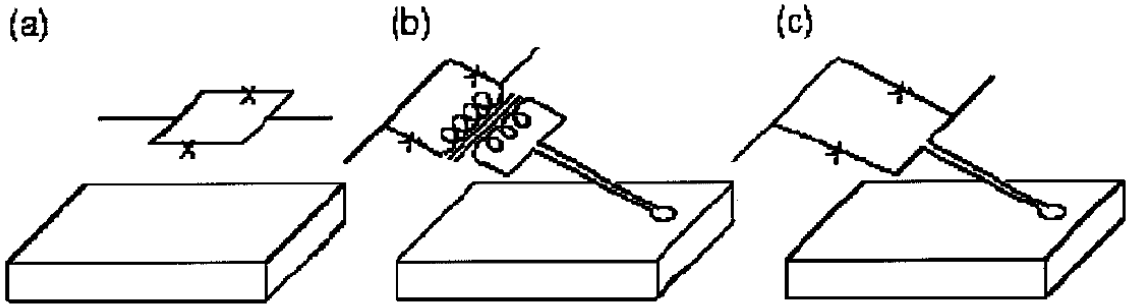

Annu. Rev. Mater. Sci. 1999. 29:117–48

Pick-up loop scanning SQUIDs

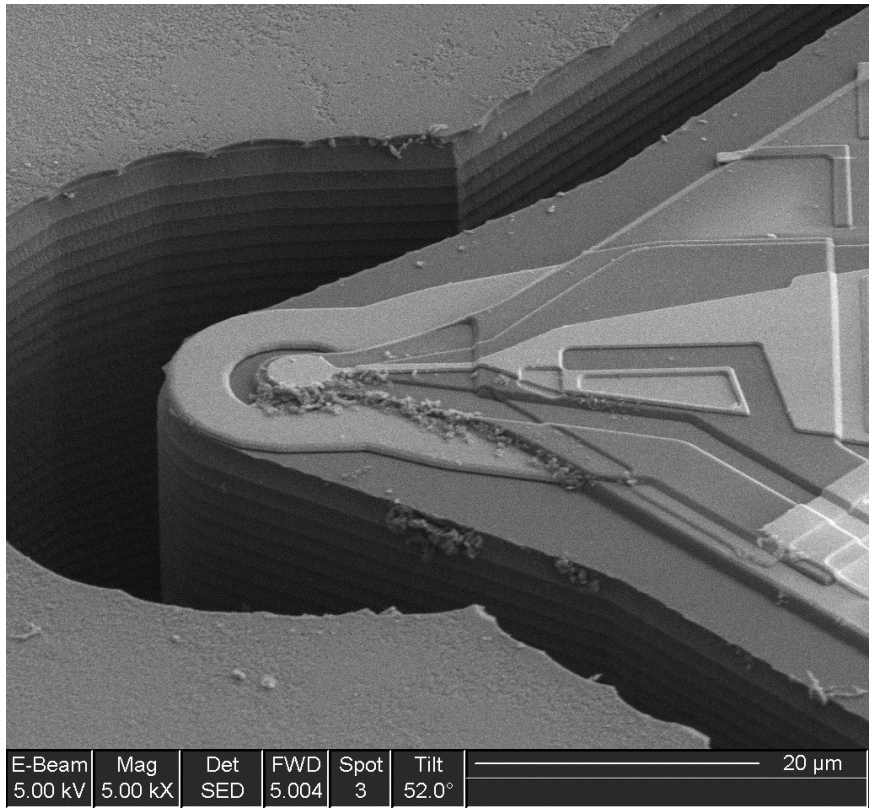

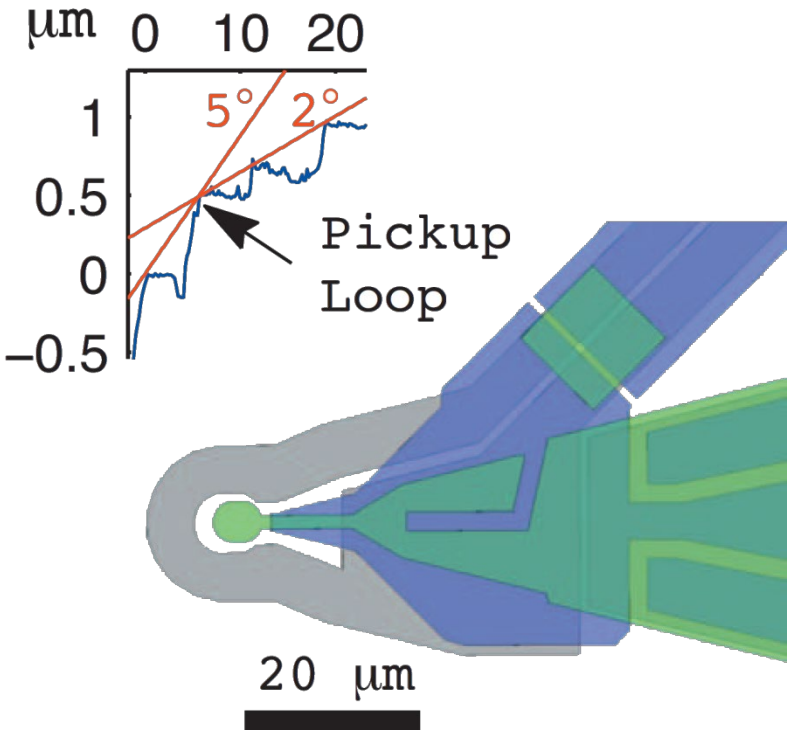

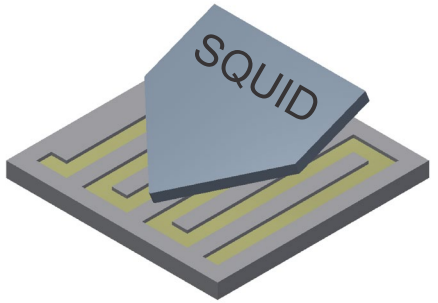

- Spatial resolution ~ 1 µm
- Field sensitivity ~ 130 nT $Hz^{-1/2}$
- ~ 400 nm to the sample

Koshnick et al., APL **93**, 243101 (2008)
Kirtley et al., RSI **87**, 093702 (2016)

Self-Aligned Nanoscale SQUID on a Tip

Amit Finkler,[*,†] Yehonathan Segev,[†] Yuri Myasoedov,[†] Michael L. Rappaport,[†] Lior Ne'eman,[†] Denis Vasyukov,[†] Eli Zeldov,[†] Martin E. Huber,[‡] Jens Martin,[§] and Amir Yacoby[§]

[†]Department of Condensed Matter Physics, Weizmann Institute of Science, Rehovot 76100, Israel, [‡]Departments of Physics and Electrical Engineering, University of Colorado, Denver, Colorado 80217, and [§]Department of Physics, Harvard University, Cambridge, Massachusetts 02138

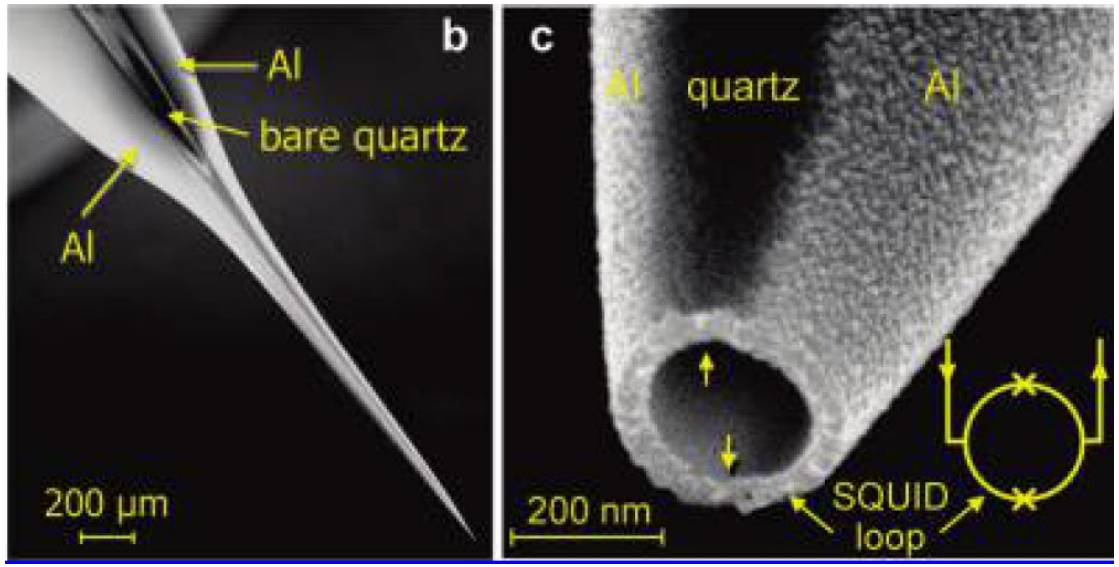

Nano Lett. **2010,** *10,* 1046–1049

Intial results show great potential

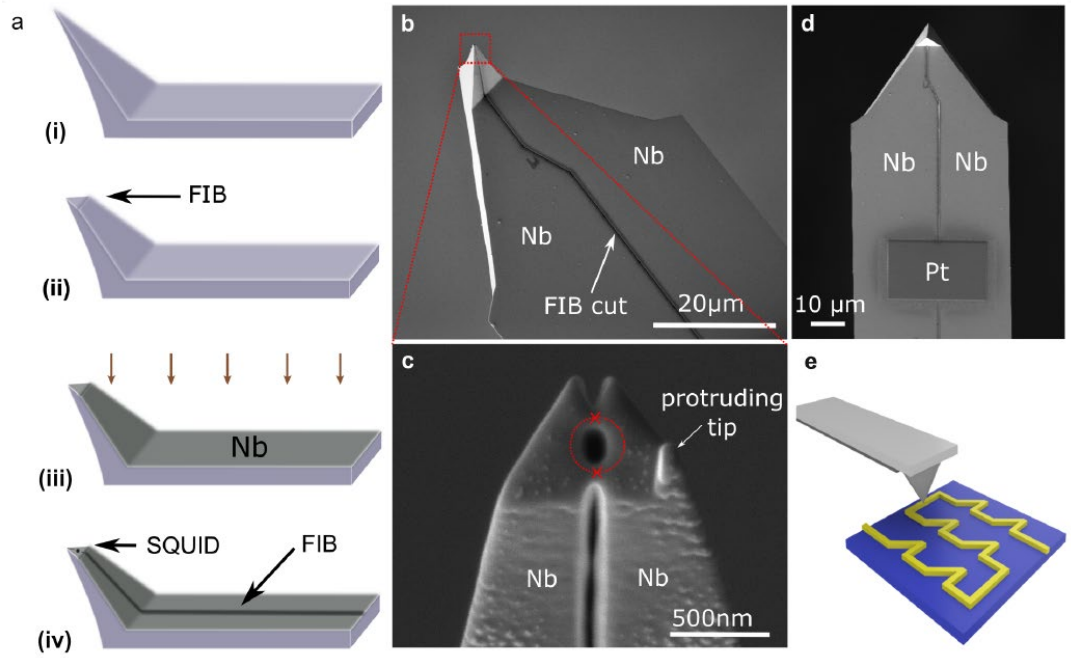

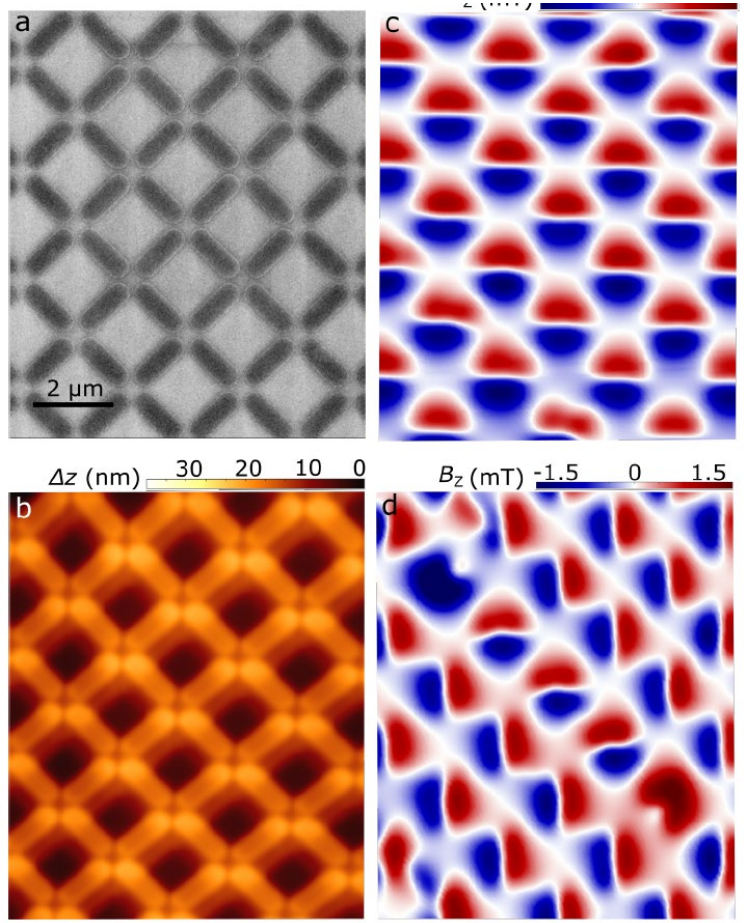

Scanning SQUID Microscopy

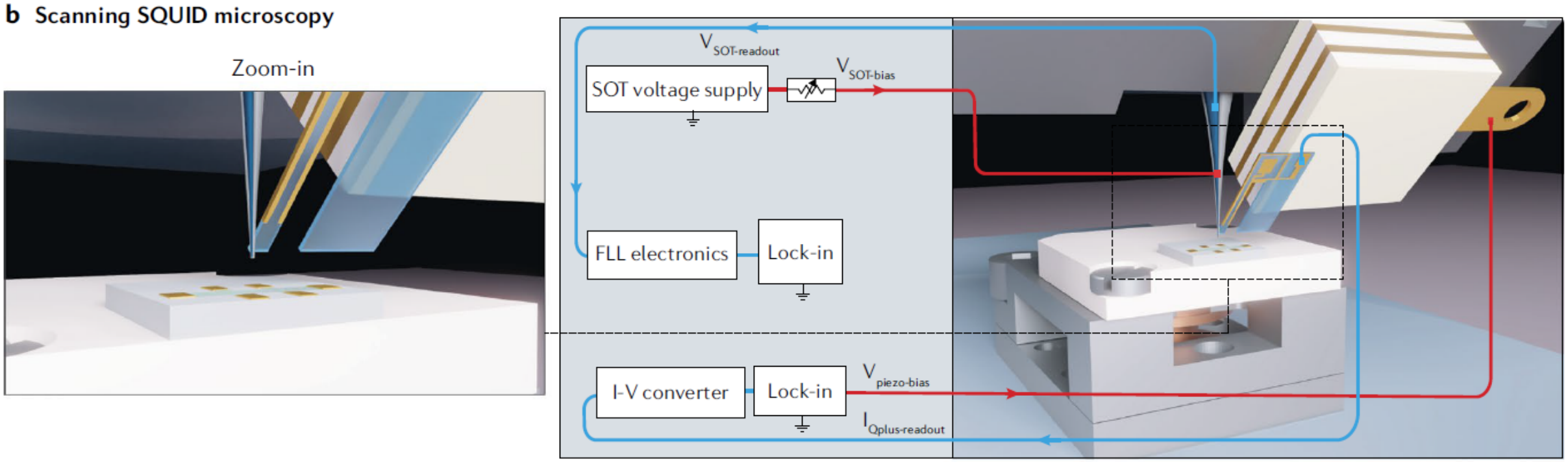

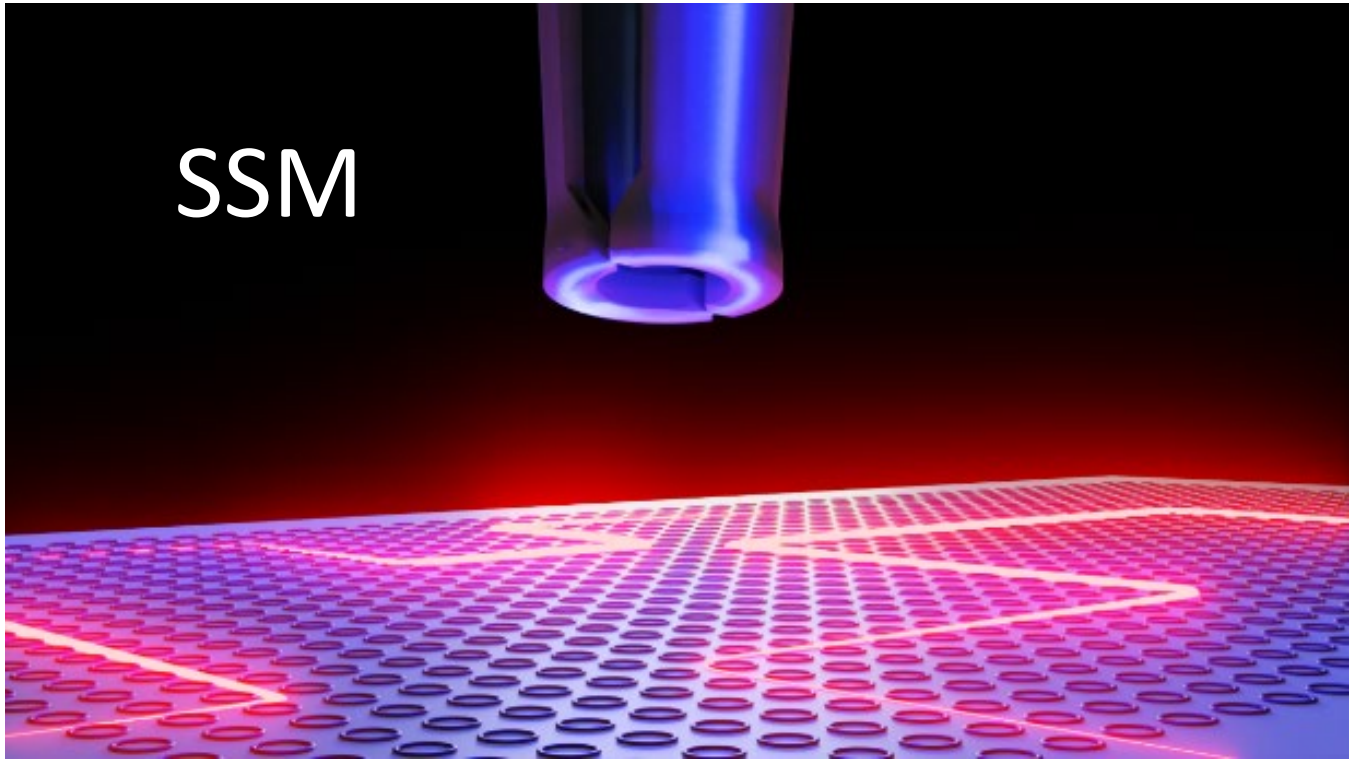
SSM

Scanning Nitrogen-vacancy Center Microscopy (SNVM)

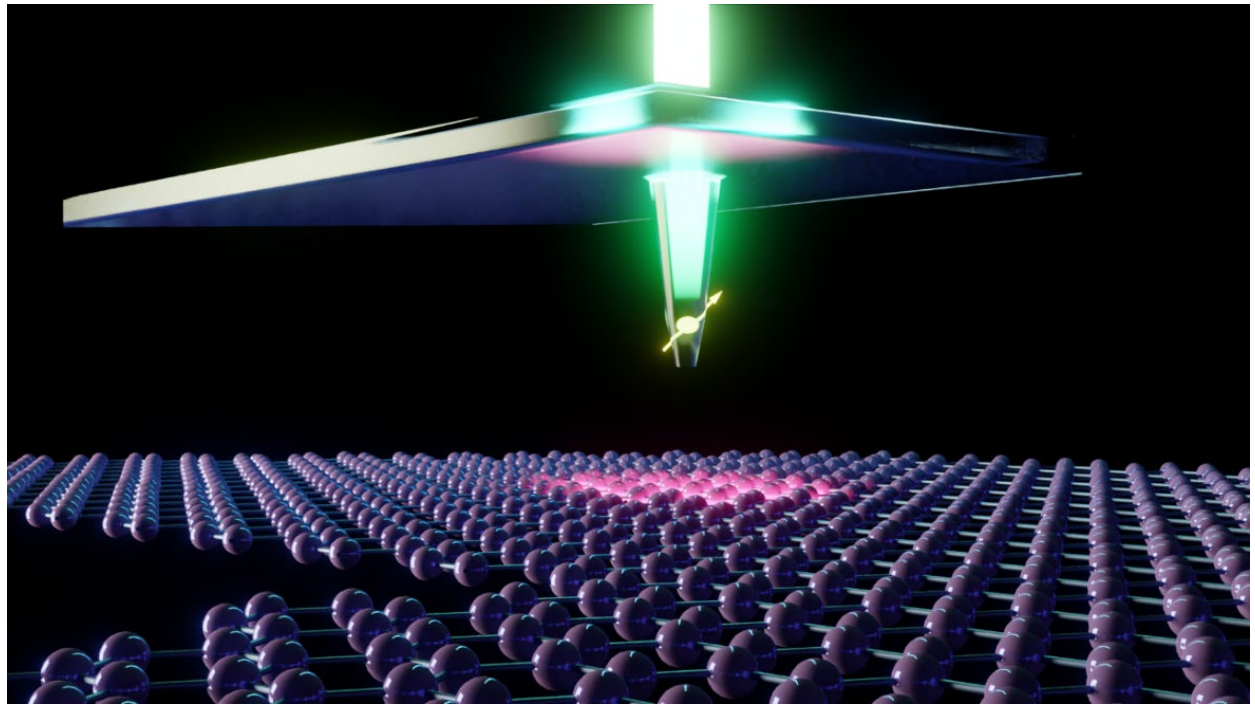

Sensitivity down to 100 nT/$(Hz)^{1/2}$

Spatial resolution down to 10 nm

Imaging current with SNVM

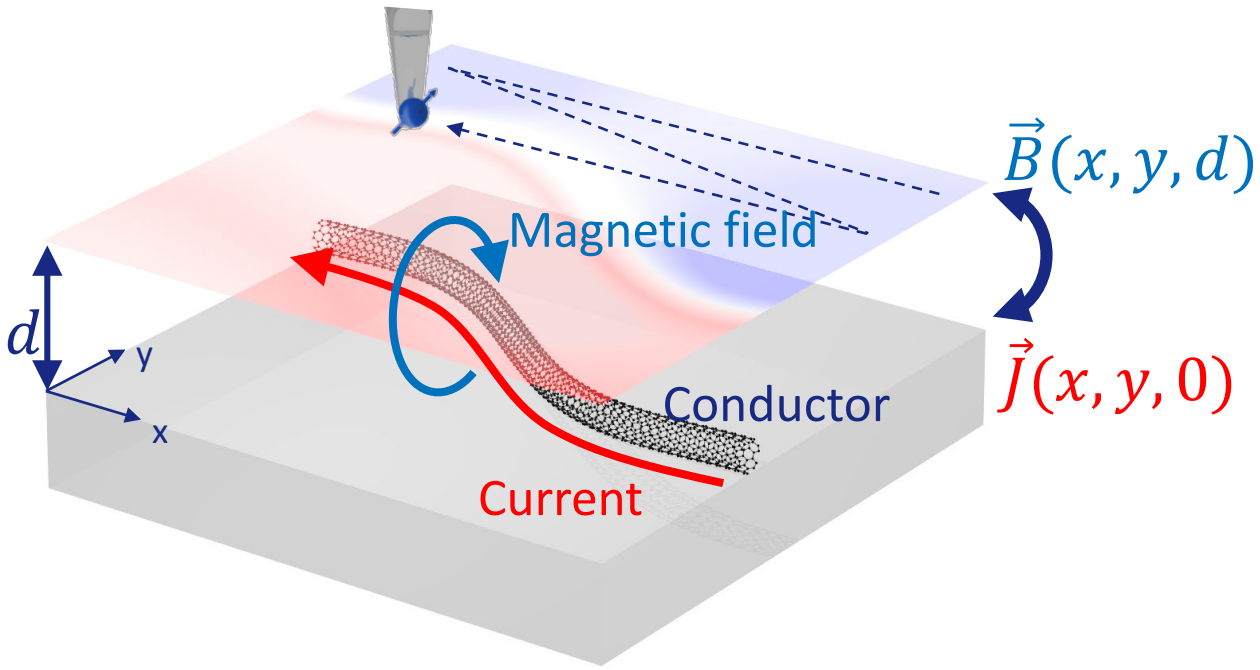

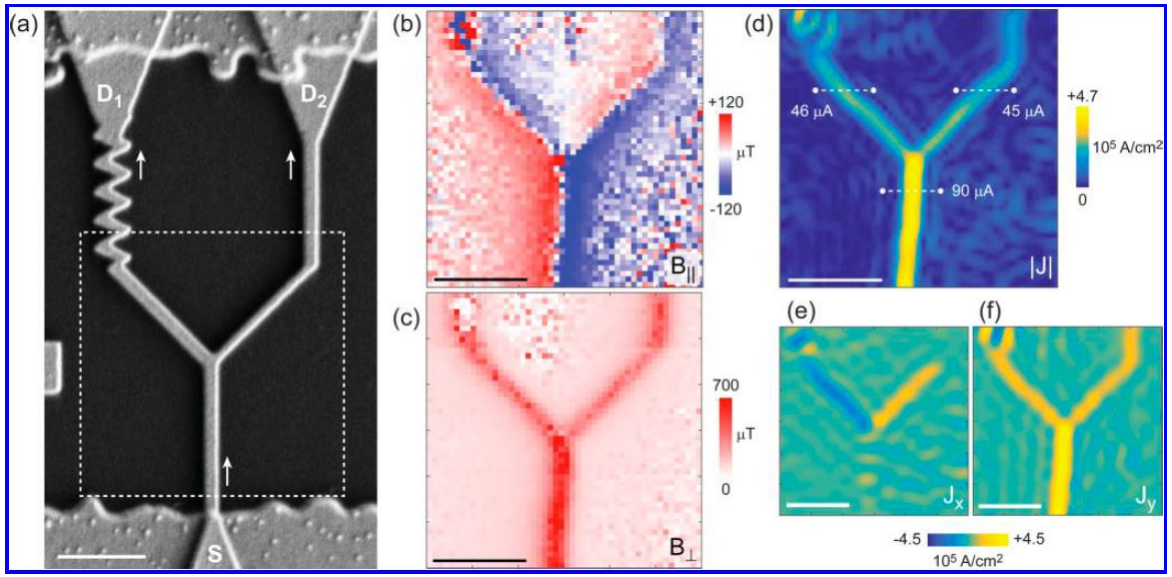

Chang et al., *Nano Lett.* **17**, 2367 (2017).

Scanning NV microscopy of 2D magnets

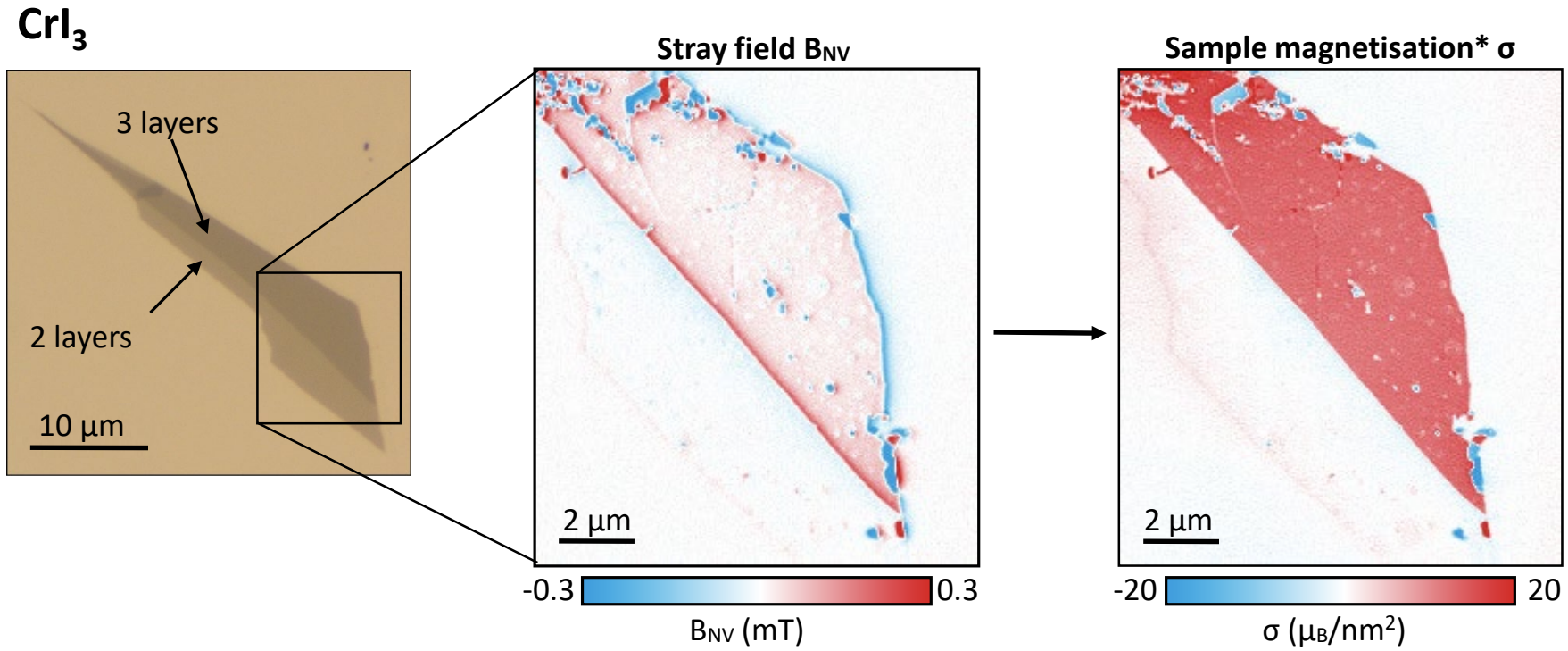

Thiel et al., *Science* **364**, 973 (2019).

Scanning NV Microscopy

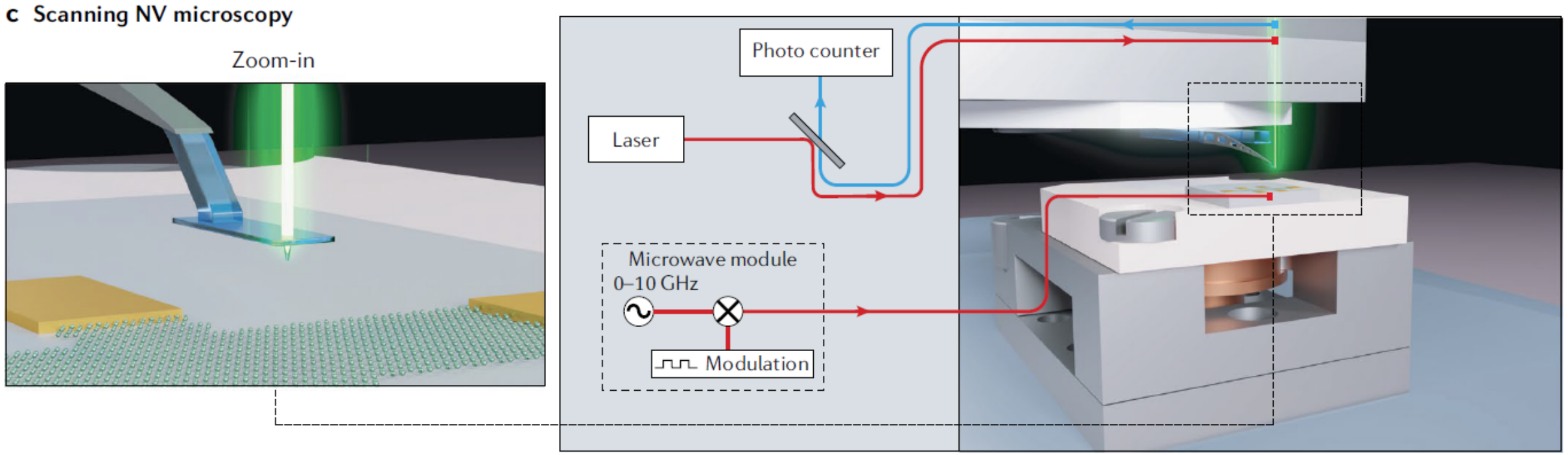

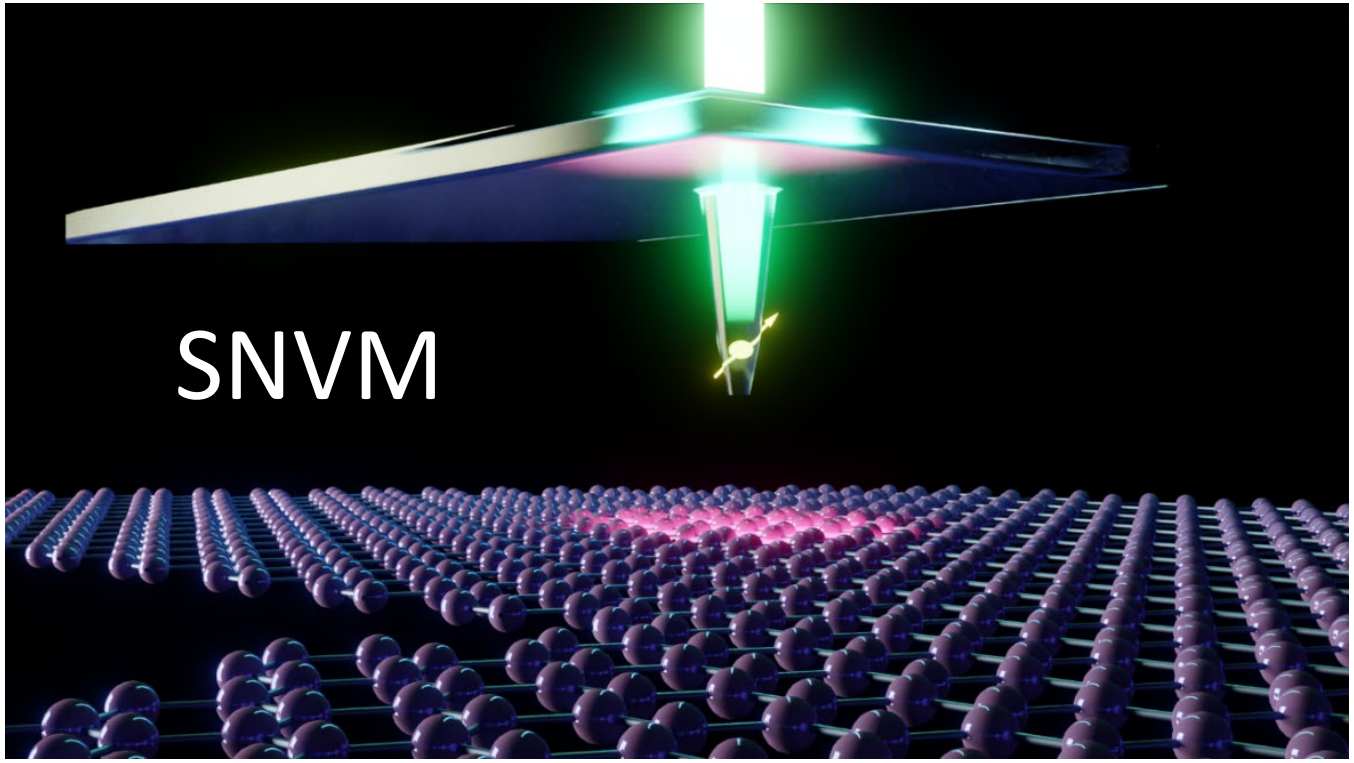
SNVM

Contrast & Techniques

Current density $\vec{J}$

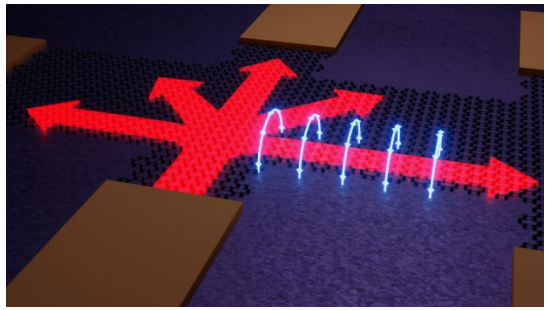

Magnetization $\vec{M}$

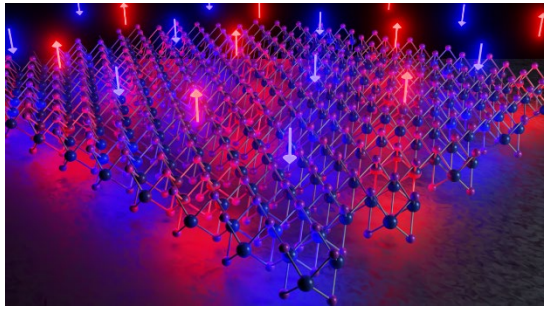

Magnetic field $\vec{B}$

SSM

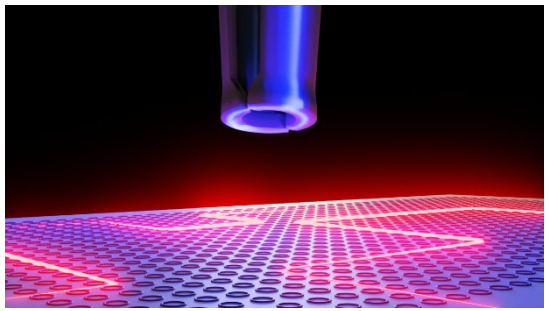

Magnetic flux Φ_z

MFM

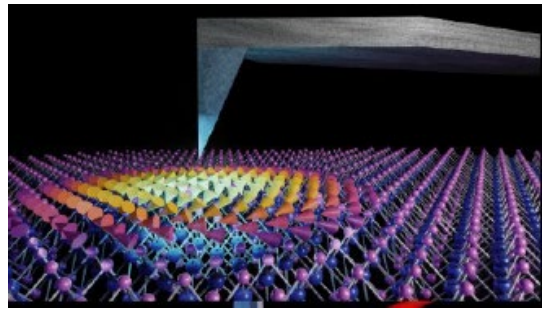

Magnetic field derivative $\frac{\partial B_z}{\partial z}$

SNVM

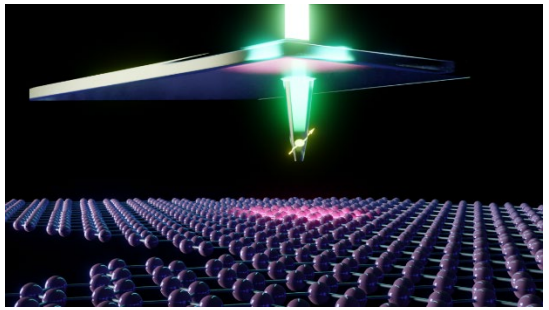

Magnetic field component B_z

Probe-sample Spacing

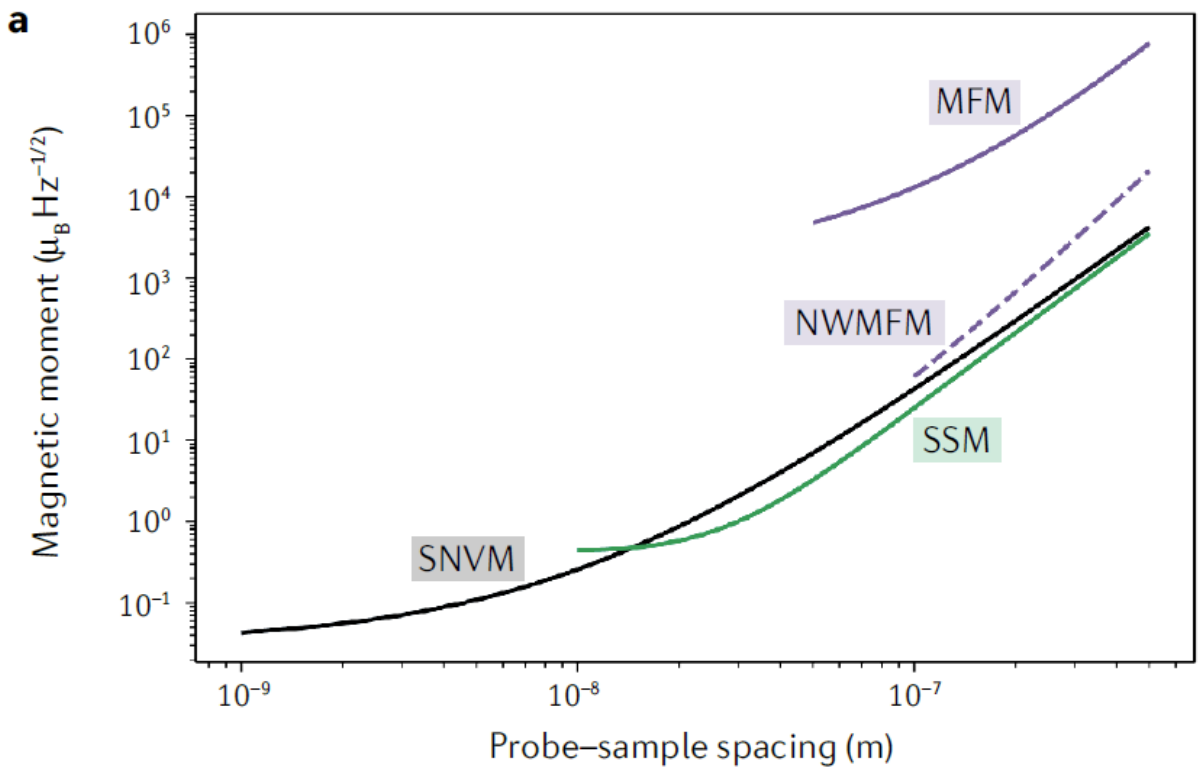

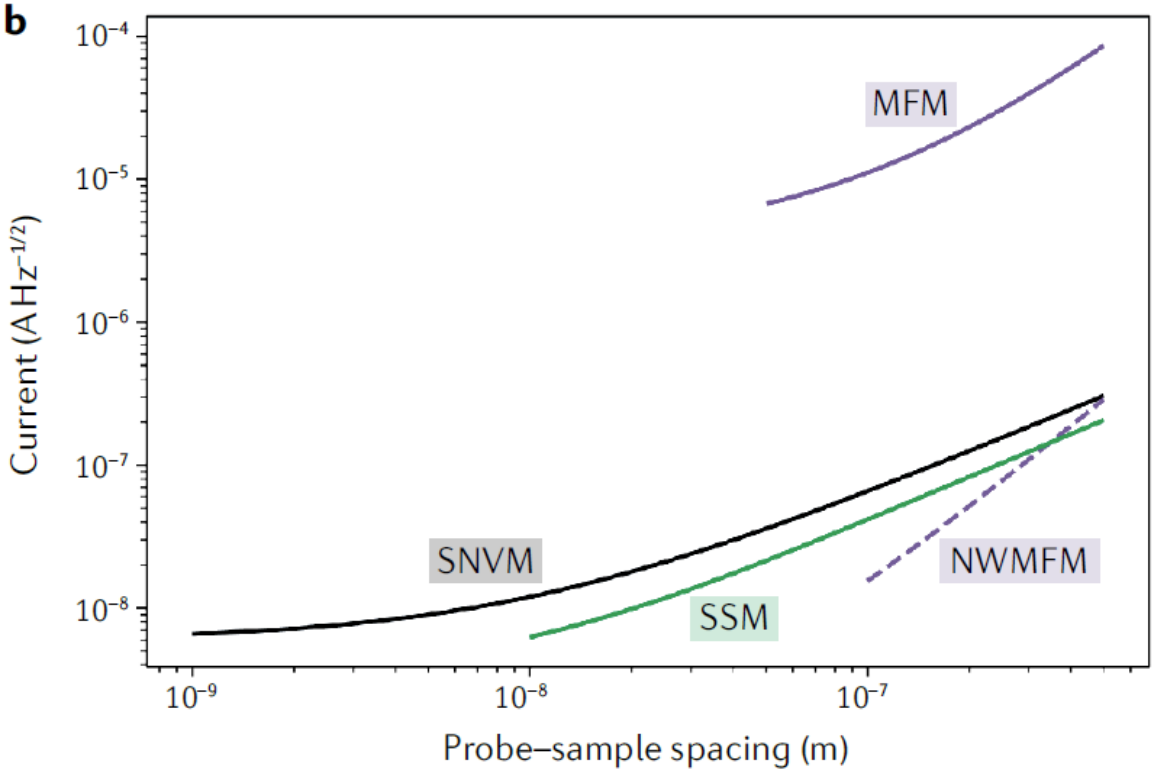

Sensor Size

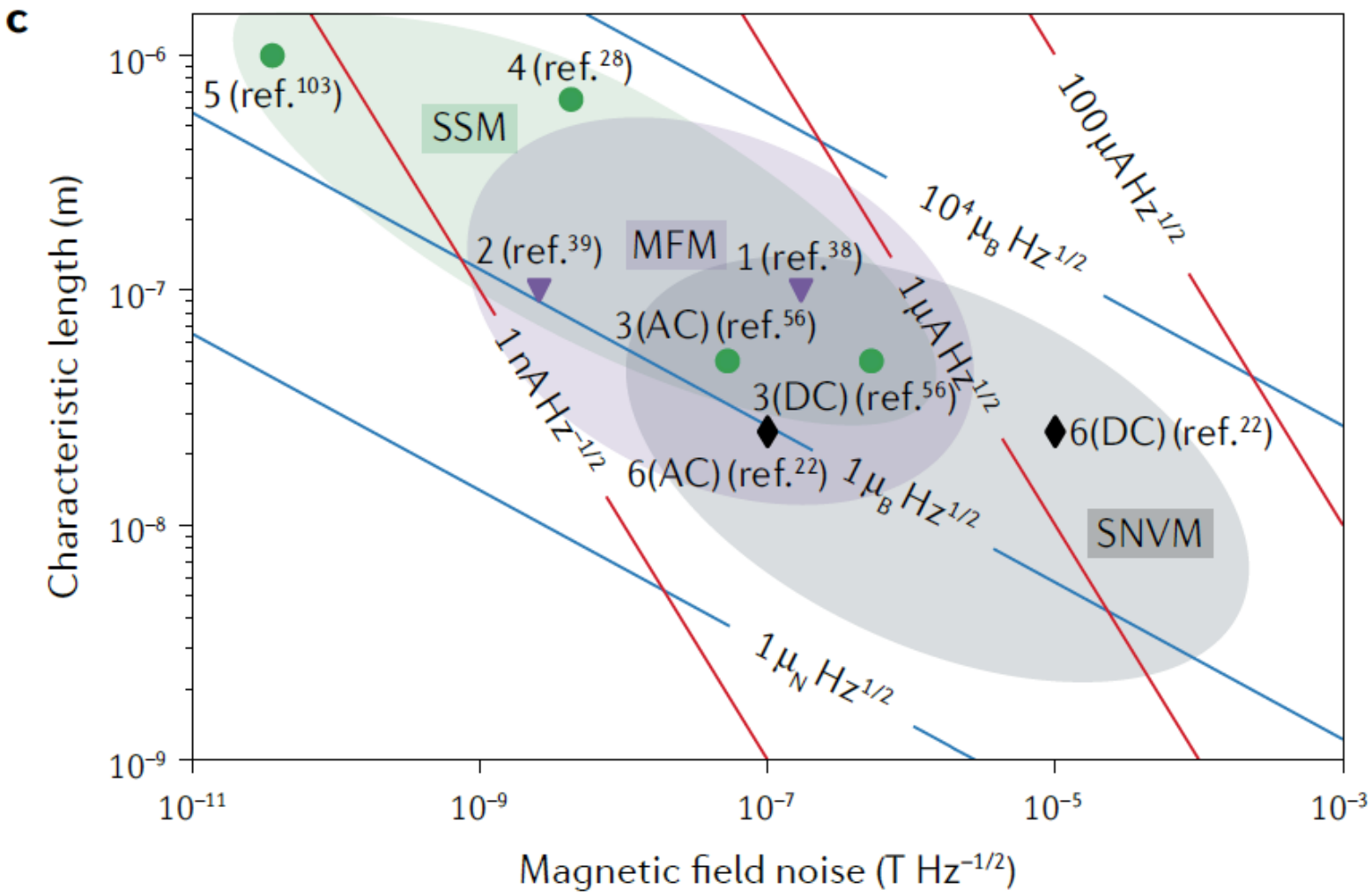
c
Characteristic length (m)
Magnetic field noise (T Hz$^{-1/2}$)
10^{-6}
10^{-7}
10^{-8}
10^{-9}
10^{-11}
10^{-9}
10^{-7}
10^{-5}
10^{-3}
5 (ref.[103])
4 (ref.[28])
SSM
2 (ref.[39])
MFM
1 (ref.[38])
3(AC) (ref.[56])
3(DC) (ref.[56])
6(AC) (ref.[22])
6(DC) (ref.[22])
SNVM
100 μA Hz$^{1/2}$
10^4 μ_B Hz$^{1/2}$
1 μA Hz$^{1/2}$
1 nA Hz$^{1/2}$
1 μ_B Hz$^{1/2}$
1 μ_N Hz$^{1/2}$

Properties

Table 1 | **Parameters for state-of-the-art magnetic scanning probe microscopies combining the highest sensitivity with the highest resolution**

	MFM (conventional)[31,32,38,102–104]	MFM (nanowire)[39]	SSM (susceptometer)[53]	SSM (SQUID-on-tip)[56]	SNVM[22,74,82,83]
Sensor size	10–100 nm	100 nm	0.5 μm	50 nm	<1 nm
Sensor stand-off	10–100 nm	50 nm	330 nm	25 nm	50 nm
Spatial resolution	10–100 nm	100 nm[a]	0.5 μm	100 nm	15–25 nm
DC sensitivity	10–100 $\mu T\,Hz^{-1/2}$	3 $nT\,Hz^{-1/2}$[a]	660 $nT\,Hz^{-1/2}$	50 $nT\,Hz^{-1/2}$	4 $\mu T\,Hz^{-1/2}$
AC sensitivity	170 $nT\,Hz^{-1/2}$	3 $nT\,Hz^{-1/2}$	130 $nT\,Hz^{-1/2}$	5 $nT\,Hz^{-1/2}$	100 $nT\,Hz^{-1/2}$
Operating field	<20 T	<10 T	<30 mT	<1.2 T	<hundreds of mT
Operating temperature	<500 K	<300 K	<9 K	<7 K	<600 K

MFM, magnetic force microscopy; SNVM, scanning nitrogen-vacancy microscopy; SQUID, superconducting quantum interference device; SSM, scanning SQUID microscopy. [a]Represents estimates based on the properties of the sensors, which have not yet been experimentally confirmed.

Sensitivity as a function of feature size

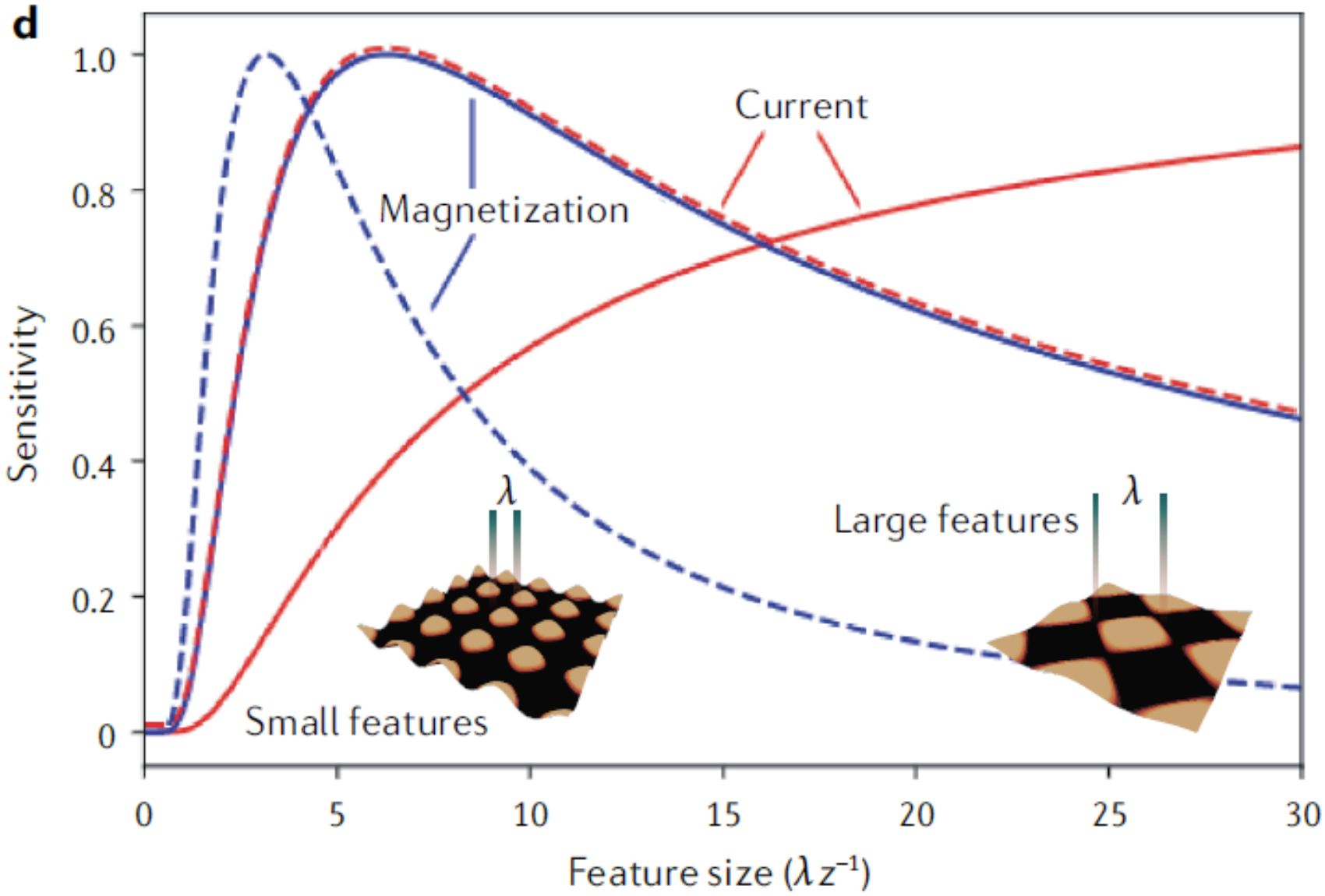

References

- Reviews on scanning magnetic field probes
  - *Nat. Rev. Phys.* **4**, 49 (2022).
  - *Rep. Prog. Phys.* **73**, 126501 (2010)
  - *Rev. Mod. Phys.* **92**, 021001 (2020)
- Current and magnetization reconstruction
  - *Nano Lett.* **17**, 2367 (2017)
  - *J. Geophys. Res.* **114**, B06102 (2009)
  - *J. Appl. Phys.* **65**, 361 (1989)

Nanoscale magnetic field imaging for 2D materials

Estefani Marchiori[1], Lorenzo Ceccarelli[1], Nicola Rossi[1], Luca Lorenzelli[2], Christian L. Degen[2] and Martino Poggio[1,3]

***Colloquium*: Quantum limits to the energy resolution of magnetic field sensors**

Morgan W. Mitchell

ICFO—Institut de Ciencies Fotoniques, The Barcelona Institute of Science and Technology, 08860 Castelldefels, Barcelona, Spain and ICREA—Institució Catalana de Recerca i Estudis Avançats, 08010 Barcelona, Spain

Silvana Palacios Alvarez

ICFO—Institut de Ciencies Fotoniques, The Barcelona Institute of Science and Technology, 08860 Castelldefels, Barcelona, Spain

Fundamental studies of superconductors using scanning magnetic imaging

J R Kirtley

Nanoscale Imaging of Current Density with a Single-Spin Magnetometer

K. Chang, A. Eichler, J. Rhensius, L. Lorenzelli, and C. L. Degen*

Obtaining vector magnetic field maps from single-component measurements of geological samples

Eduardo A. Lima[1] and Benjamin P. Weiss[1]

Using a magnetometer to image a two-dimensional current distribution

Bradley J. Roth,[a] Nestor G. Sepulveda, and John P. Wikswo, Jr.

Living State Physics Group and Vanderbilt Electromagnetics Laboratory, Department of Physics and Astronomy, Vanderbilt University, Nashville, Tennessee 37235